

Laboratory Observation of the Buffering Effect of Aragonite Dissolution at the Seafloor

**Key Points:**

- The effects of aragonite dissolution at the sediment-water interface were measured during short-term laboratory experiments
- Measured porewater pH micro-profiles and a diagenetic model were used to isolate the effects of each reaction on porewater pH
- Our experiments and simulations suggest that aragonite dissolution, through its buffering effect, slows, and eventually suppresses calcite dissolution

Supporting Information:

Supporting Information may be found in the online version of this article.

Correspondence to:








H. van de Mortel and O. Sulpis,
vandemortel.hanna@gmail.com;
sulpis@cerege.fr

Citation:

van de Mortel, H., Delaigue, L., Humphreys, M. P., Middelburg, J. J., Ossebaar, S., Bakker, K., et al. (2024). Laboratory observation of the buffering effect of aragonite dissolution at the seafloor. *Journal of Geophysical Research: Biogeosciences*, 129, e2023JG007581. <https://doi.org/10.1029/2023JG007581>

Received 16 MAY 2023

Accepted 5 FEB 2024

H. van de Mortel¹ , L. Delaigue² , M. P. Humphreys² , J. J. Middelburg¹ , S. Ossebaar², K. Bakker², J. P. Trabucho Alexandre¹ , A. W. E. van Leeuwen-Tolboom¹, M. Wolthers¹ , and O. Sulpis^{1,3} 

¹Department of Earth Sciences, Utrecht University, Utrecht, The Netherlands, ²Department of Ocean Systems (OCS), NIOZ Royal Netherlands Institute for Sea Research, Texel, The Netherlands, ³CEREGE, Aix Marseille University, CNRS, IRD, INRAE, Collège de France, Aix-en-Provence, France

Abstract Carbon dioxide entering and acidifying the ocean can be neutralized by the dissolution of calcium carbonate, which is mainly found in two mineral forms. Calcite is the more stable form and is often found in deep-sea sediments, whilst aragonite is more soluble and therefore rarely preserved. Recent research shows aragonite may account for a much larger portion of marine calcium carbonate export to the ocean interior via the biological pump than previously thought, and that aragonite does reach the deep sea and seafloor despite rarely being buried. If aragonite is present and dissolving at the seafloor it will raise local pH and calcium and carbonate concentrations, potentially enough to inhibit calcite dissolution, representing a deep-sea, carbonate version of galvanization. Here, we test this hypothesis by simulating aragonite dissolution at the sediment-water interface in the laboratory and measuring its effects on pH using microsensors. We show that the addition of aragonite to calcite sediment, overlain by seawater undersaturated with respect to both minerals, results in an unchanged alkalinity flux out of the dissolving sediment, suggesting a decrease the net dissolution rate of calcite. In combination with a diagenetic model, we show that aragonite dissolution can suppress calcite dissolution in the top millimeters of the seabed, locally leading to calcite precipitation within 1 day. Future research efforts should quantify this galvanization effect in situ, as this process may represent an important component of the marine carbon cycle, assigning a key role to aragonite producers in controlling ocean alkalinity and preserving climatic archives.

Plain Language Summary Carbon dioxide (CO₂) concentrations are rising due to human influences and the ocean takes up around a third of these CO₂ emissions, causing ocean acidification. This can be counteracted by dissolving calcium carbonate (CaCO₃), which neutralizes CO₂. CaCO₃ makes up the shells of organisms living in surface waters, which sink to the bottom after dying. Most deep-sea sediments are made up of a stable form of CaCO₃ called calcite. However, there is increasing evidence that a more soluble form of CaCO₃ called aragonite also reaches the seafloor. If aragonite does reach the seafloor, its dissolution could protect the surrounding calcite grains from dissolving. This has been shown in a computational study by Sulpis, Agrawal, et al. (2022), <https://doi.org/10.1038/s41467-022-28711-z>, and is further demonstrated in this laboratory study, where we dissolved aragonite on a calcite bed and measured the surrounding seawater chemistry at sub-millimeter scale. Our study suggests that aragonite not only protects calcite from dissolution, but also leads it to grow. This indicates that aragonite plays an important role in CO₂ neutralization and should be included in any representation of the marine carbon cycle.

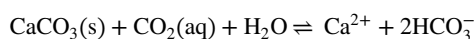
1. Introduction

The marine CaCO₃ cycle regulates the uptake, storage and release of carbon dioxide (CO₂) to the atmosphere and therefore plays an important role in controlling atmospheric CO₂ on millennial timescales. The current buffering of anthropogenic CO₂ serves as a good example: the global ocean has absorbed approximately one-third of anthropogenic CO₂ emissions in recent years (Friedlingstein et al., 2022; Gruber et al., 2019). The ocean's large storage capacity of inorganic carbon results from the reaction of carbon dioxide (CO₂) with water to form bicarbonate (HCO₃⁻) and carbonate (CO₃²⁻) ions, releasing protons (H⁺), which lowers pH. Changes in the distribution of the dissolved carbonate species chemically buffer seawater against the effects of CO₂ addition. Homogenous buffering involves only dissolved components, whereas heterogenous buffering also includes the balance between precipitation and dissolution of carbonate minerals (Middelburg, 2019). The latter is termed

© 2024. The Authors.

This is an open access article under the terms of the [Creative Commons Attribution License](https://creativecommons.org/licenses/by/4.0/), which permits use, distribution and reproduction in any medium, provided the original work is properly cited.

geochemical carbonate compensation, and allows CO₂ entering the ocean to be neutralized by CaCO₃ dissolution (Plummer et al., 1978):



In the open ocean, most CaCO₃ originates from the shells and skeletons of various organisms living in surface waters (Smith & Mackenzie, 2016). These biominerals are exported from surface waters via multiple pathways, including incorporation into marine snow aggregates and fecal pellets (Richardson, 2019; Silver et al., 1978), and they sink to the seafloor due to gravity. The global CaCO₃ delivery flux to oceanic sediments is estimated to range from 40 to 60 Tmol yr⁻¹, amongst which 11–12 Tmol will be preserved and buried, the rest being dissolved during early diagenesis (Sulpis et al., 2021). Because deep-sea carbonate minerals cover most of the seafloor (Milliman, 1993), they are thus fundamental to regulating atmospheric CO₂.

The saturation state (Ω) of seawater with respect to each CaCO₃ mineral is the driving force behind the mineral's precipitation or dissolution. If $\Omega = 1$, the solid and solution are in equilibrium; if $\Omega < 1$, the solution is undersaturated and mineral dissolution can occur; and if $\Omega > 1$, the solution is supersaturated and precipitation should occur. The saturation state is given by

$$\Omega = \frac{[\text{Ca}^{2+}][\text{CO}_3^{2-}]}{K_{\text{sp}}^*}$$

where square brackets are concentrations and K_{sp}^* is the stoichiometric solubility constant, a function of salinity, temperature and pressure that is specific to each calcium carbonate mineral (Mucci, 1983). Whilst dissolved calcium is uniformly distributed throughout the global ocean due to its long residence time (1.1·10⁶ yr; Broecker & Peng, 1982), carbonate ion concentration is subject to strong short-scale changes, both spatially and temporally (Takahashi et al., 2014), and therefore plays an important role in controlling the saturation state variability in seawater. Low saturation states in the deep ocean are explained by higher CaCO₃ solubility at high pressure and low temperature (Millero, 1979) and, to a lesser extent, by changes in carbonate ion concentration (Berelson et al., 1997) caused by the buildup of CO₂ in deep waters due to the oxidation of organic matter (Volk & Hoffert, 1985). The depth where seawater first becomes undersaturated ($\Omega < 1$) with respect to a carbonate mineral is termed the saturation depth for that mineral. Below their saturation depths, dissolution rates of CaCO₃ minerals generally increase with depth due to the decreasing Ω (Schink & Guinasso, 1977; Takahashi & Broecker, 1977). In the ocean, different CaCO₃ minerals are found, each with its own composition or crystal structure, hence, with its own solubility and saturation depth.

The most stable polymorph of calcium carbonate under Earth-surface conditions is calcite, which in the open ocean constitutes the shells of the unicellular coccolithophores (phytoplankton) and planktonic foraminifera (zooplankton). Calcite is often the only polymorph found in deep-sea sediments and most sediment traps (Bernier & Honjo, 1981; Buitenhuis et al., 2019; Fabry, 1990; Fabry & Deuser, 1991). Aragonite is the second most stable polymorph of CaCO₃ and its pelagic production is dominated by planktonic gastropods living in surface waters (Lalli & Gilmer, 1989). Most biogeochemical models used to project and reconstruct Earth's climate treat all CaCO₃ as calcite (Aumont et al., 2015; Ilyina et al., 2013; Moore et al., 2013; Watanabe et al., 2011). However, recent research suggests aragonite export could be at par with that of calcite, which is a much larger contribution than initially thought (Bednaršek et al., 2012; Bernier, 1977; Buitenhuis et al., 2019; Gangstø et al., 2008).

Aragonite is about 50% more soluble than calcite (Mucci, 1983). Thus, in all oceanic regions, the aragonite saturation depth (~2,500 m in the Atlantic, ~300 m in the Northern Pacific; Feely et al., 2004) is shallower than the calcite saturation depth (~4,000 m in Atlantic, ~500 m in the Northern Pacific; Feely et al., 2004). The difference in the depth of the saturation level between the Atlantic and Northern Pacific is due to the pattern of the thermohaline circulation, Northern Pacific deep waters being older and having accumulated more metabolic CO₂ than the young and recently ventilated Northern Atlantic deep waters. Because most of the seafloor is deeper than the aragonite saturation depth, aragonite is rarely preserved at the seafloor (Berger, 1978). However, sediment traps have recorded high concentrations of pteropod genetic material (Boeuf et al., 2019) and aragonite grains (Dong et al., 2019) at abyssal depths. This suggests that aragonite does reach the seafloor despite rarely being buried there. Presumably, it dissolves at or near the sediment-water interface (SWI), where it could affect the

Table 1
Overview of the Two Experiments Conducted

	Calcite sand	Aragonite material	Initial composition of overlying seawater	Container	Hydrodynamics	Duration	Goal
Experiment 1: rotating disk reactor experiment (RDR)	Foraminifera ooze deposit	Spherical coral fragments	$\Omega_{ca} = 0.3 \pm 0.04$ $TA = 681 \pm 5.4 \mu\text{mol kg}^{-1}$	Rotating disk reactor (radius = 7.5 cm, height sediment disk = 3 cm, height reactor = 12 cm)	Reproduced hydrodynamics of an abyssal SWI	64 days	Measure changes in dissolution-generated alkalinity flux through the SWI when various amounts of aragonite are added on a calcite bed
Experiment 2: cuvette experiment (CUV)	Foraminifera ooze deposit	Pteropod shells	$\Omega_{ca} = 0.3 \pm 0.04$ $TA = 681 \pm 5.4 \mu\text{mol kg}^{-1}$	Quartz cuvette (5 × 2 × 6 cm)	Absence of flow	4 days	Quantify dissolution rates of calcite and aragonite, and possibly calcite precipitation rates, at a high depth resolution using pH microprofiles and a diagenetic model

dissolution kinetics of calcite (Archer, 1996; Sulpis et al., 2018). In a sedimentary system with overlying seawater undersaturated with respect to both calcite and aragonite but containing both minerals, aragonite will dissolve fully due to it being the most soluble (Mucci, 1983), raising TA and Ω , and subsequently hampering calcite dissolution. Sulpis, Agrawal, et al. (2022) showed this effect using a 3-D, micrometric-scale reactive-transport model to simulate the dissolution of an aragonite pteropod shell on a bed of calcite particles in a typical deep-sea setting, describing it as a deep-sea, carbonate version of galvanization. However, this galvanizing effect has not yet been supported with observations.

Here, we test this hypothesis of aragonite galvanization by dissolving aragonite particles on a bed of calcite particles in the laboratory and measuring changes in pH (with microelectrode profiling) and alkalinity in both porewaters and water above the sediment. From measured alkalinity fluxes, we propose that an increase in aragonite dissolution rate causes a decrease in net calcite dissolution rate of the same magnitude. In addition, using a reactive-transport sediment model, we show that aragonite dissolution should induce calcite precipitation to explain the observed pH microprofiles. We discuss the consequences of aragonite galvanization for interpreting paleoenvironment records and water depth distributions of carbonate minerals. In the future, less aragonite accumulating at the seafloor would enhance dissolution of calcite at the seafloor and destroy associated climate archives.

2. Materials and Methods

Two complementary experiments were carried out to test the hypothesis of aragonite galvanization. (a) A 64-day long dissolution experiment was run, in which (aragonite) coral fragments were placed in a calcite bed in a rotating-disk reactor (RDR) that reproduces the hydrodynamics of the abyssal SWI, filled with undersaturated, natural water. The goal was to measure how the dissolution-generated alkalinity flux through the SWI changes when various amounts of aragonite are added onto a calcite seabed by measuring bulk seawater TA and pH porewater profiles. This experiment showed an aragonite galvanizing effect but also highlighted the need to observe porewater pH changes on much shorter, for example, hourly, timescales, and to seek for traces of calcite precipitation in a smaller, better controlled environment. Thus, another follow-up experiment was needed. (b) A 4-day long dissolution experiment was carried out, in which (aragonite) pteropod shells were placed on a calcite bed in a 5 × 2 × 6 cm quartz glass cuvette filled with undersaturated, natural seawater, in the absence of flow. The goal was to measure the effects of aragonite dissolution on pH profiles across the SWI at a high (sub-millimetric) resolution, and combining the measured profiles with a diagenetic model, to quantify the calcite and aragonite dissolution rates, and the calcite precipitation rate, if any. These two experiments are described in detail in the following, and for clarity, a summary is provided in Table 1.

2.1. Material

Natural seawater from the Marsdiep, a tidal inlet between Den Helder and Texel in the Netherlands connecting the North Sea and Wadden Sea, was filtered with Grade GF/F, 47 mm filters (down to 0.7 μm) and mixed to mask the

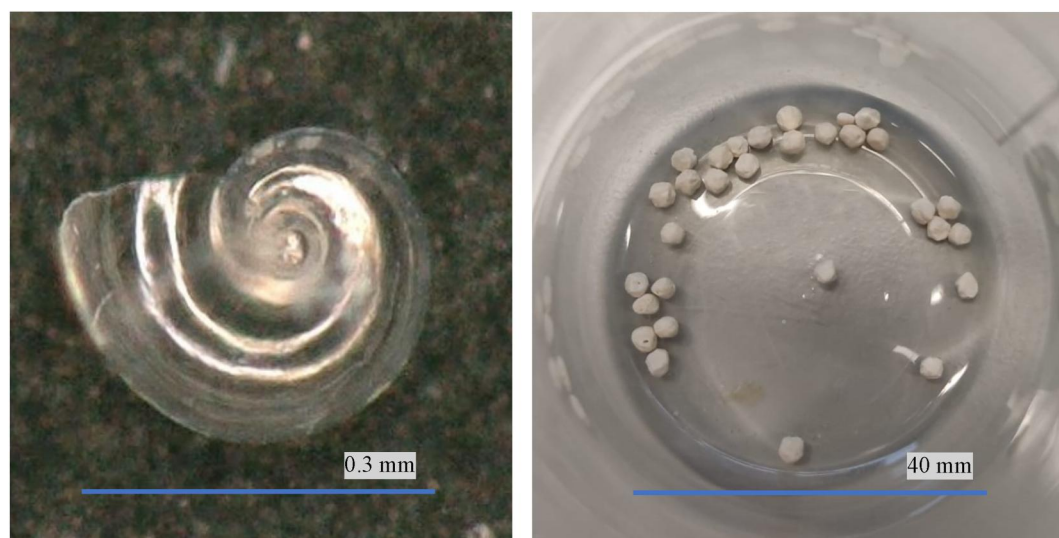


Figure 1. Left: A juvenile pteropod, photographed using a Keyence VHX-7000 digital microscope. Right: Spherical aragonite fragments.

tidal influence on water composition. In total, 70 L of water was collected and separated into seven different batches. All batches had a practical salinity of 28.3, and the mean \pm standard deviation initial TA across all batches was $2,373 \pm 1.1 \mu\text{mol kg}^{-1}$. Hydrogen chloride solution (HCl, 1 M) was added to achieve a saturation state of $\Omega_{\text{ca}} = 0.3$ for 60 L and $\Omega_{\text{ca}} = 1.0$ for the remaining 10 L of seawater. Air pumps were used to bubble air ($p\text{CO}_2 = 480 \mu\text{atm}$) through the seawater for 3 weeks until steady state was reached between the seawater and the air; steady-state was inferred from the stabilization of pH readings (pH constant within ± 0.10 for 3 consecutive days, measured using a Mettler Toledo pH Sensor InLab Expert Pro-ISM). The 60 L seawater with $\Omega_{\text{ca}} = 0.3 \pm 0.04$ ($\text{TA} = 681 \pm 5.4 \mu\text{mol kg}^{-1}$) was used for both dissolution experiments (Table 1), and had a pH_T of 7.40 ± 0.05 . The 10 L seawater with $\Omega_{\text{ca}} = 1.0 \pm 0.12$ was used for calcite sand equilibration, explained below.

A foraminiferal ooze deposit from the Walvis Ridge (-29.74 N , 2.29 E) from 2,896 m depth and 6 m below the SWI, was wet-sieved ($63 \mu\text{m}$) and dried at room temperature to provide calcite sand (with a porosity of 40%, determined by the difference in weight between the wet and dry calcite sand, which is converted to volume and then divided by the total volume of the wet calcite). The calcite sand was pre-equilibrated in the 10 L of seawater ($\Omega_{\text{ca}} = 1.0 \pm 0.12$, $\text{TA} = 1,093 \pm 4.0 \mu\text{mol kg}^{-1}$, $\text{pH}_T = 7.71 \pm 0.05$), regularly stirred, for 2 weeks to dissolve any mineral phases more soluble than pure calcite. X-Ray Powder Diffraction (XRPD) (methodology in Section 2.4.4) showed that the calcite sand consisted of 96% calcite, 4% feldspar and trace amounts of quartz and halite (the latter formed during drying) (Table A4 in Supporting Information S1). This sand is hereafter referred to as the “calcite sand”.

Juvenile pteropod shells (Figure 1) were taken from the shallow waters of the western entrance of the Corinth Channel in Greece. Surface water from the Corinth Channel was pumped and filtered through a net ($75 \mu\text{m}$ mesh) for several hours. The retrieved pteropods were frozen, freeze-dried, and organic material was removed using a Low Temperature Asher. No quantitative mineralogical analysis was possible for the pteropod sample due to the low amount of sample available. However, the composition was inferred from initial qualitative results and quantitative XRPD results done after the first experiment, indicating approximately 48% aragonite, 50% calcite, and 2% quartz. The pteropods were only used for the cuvette experiments, and not in the RDR experiment (Table 1). This was due to a limited amount of pteropods being available, as well as their small size making them difficult to manage. Instead, spherical aragonite fragments (Figure 1) were used for the RDR experiment. These were created by breaking coral branches into small pieces and filing them manually into 1–2 mm diameter spheres. The coral originated from the Rockall Bank, Logachev mound province at 550–1,000 m water depth and was collected via box cores.

Seawater was not poisoned with mercuric (II) chloride, but instead filtered to limit microbial respiration. To test the effects of microbial activity on seawater carbonate chemistry during the timespan of our experiments, two

beakers were filled with calcite sand and filtered seawater. Mercuric chloride was added (100 μg of mercuric chloride per milliliter of sample) to one beaker to inhibit any biological activity. O_2 concentration was measured at five different depths (1.5 and 0.5 above the SWI, 0.5, 1.5, and 2.5 cm below the SWI) using Unisense microelectrodes. These profiles were done again after 4 days and then again after another 3 days to see if any oxygen was consumed or produced. No detectable change in $[\text{O}_2]$ was observed at 1.5, 0.5, and -0.5 cm depth. At -1.5 cm and -2.5 cm, both the poisoned and the non-poisoned beaker showed some $[\text{O}_2]$ consumption after 7 days (Figure A1 in Supporting Information S1). We conclude that it is unlikely that microbial respiration affected our experimental results substantially within 7 days, but it is possible that it had an effect on longer periods.

2.2. Experiment 1: Rotating Disk Reactor

2.2.1. Rotating Disk Reactor

Rotating disk reactors (RDR) are used to precisely control mass transfer conditions at the interface between a liquid and a dissolving solid. They have been used in the context of calcite dissolution in seawater (Sjöberg & Rickard, 1983, 1984a, 1984b; Sulpis et al., 2019), notably, to reproduce in the laboratory the slow bottom-water current speed of the seafloor, and precisely control the diffusive boundary layer (DBL) thickness at the SWI in the laboratory. The DBL is a thin film of water extending up to a few millimeters above the SWI in which molecular diffusion is the dominant mode of solute transport (Boudreau & Guinasso, 1982). Reproducing this DBL in the laboratory is important when simulating benthic diffusive fluxes, since the thick diffusive boundary layers often seen at the sea floor significantly reduce the diffusive rate of solutes through the SWI. The RDR simulates slow flow in a reaction chamber filled with seawater using a rotating sediment disk (Figure A2 in Supporting Information S1), where the entire water velocity gradient is reproduced from zero velocity at the SWI to constant full velocity at the top of the water level. Here, we do not aim to test the effect of a DBL on dissolution rates, but simply to perform experiments representative of deep-sea environments. By spinning the disk at a constant rate of two rotations per minute, the bottom-water current speed reproduces a diffusive boundary layer (DBL) thickness of 300 μm , which is representative of a typical deep-sea or shelf environment (Sulpis et al., 2018).

2.2.2. Timeframe of Experiments

The rotating disk within the reactor was filled with uniformly distributed calcite sand and then the reactor was filled with acidified seawater ($\Omega_{\text{ca}} = 0.3$), marking the start of the experiment. Using a multi-channel peristaltic pump (Gilson's Minipuls 3), seawater was pumped through the reactor chamber at a constant rate of 11.28 mL hr^{-1} via a 0.76 mm inner diameter Tygon polyvinylchloride (PVC) tube. The pumping rate was determined in each experiment by measuring the volume of solution pumped out of the reactor over a fixed period. To keep a constant volume of solution in the reactor, the solution was withdrawn from the reactor by the same pump through a wider, 1.02 mm inner diameter tube whose inlet was at a fixed height within the reactor, that is, the surface of the solution. The batch reactor was capped by a lid with openings for the solution input and output tubes and a combination glass-reference pH electrode.

The evolution of the dissolution reaction was assessed by monitoring daily the pH of the experimental solution in the water overlying the sediments inside the reactor at a fixed acidified-seawater pumping rate. At the beginning of the experiment, pH increased due to the dissolution of the calcite sand. Then, the dissolution was eventually high enough to balance the acidification caused by pumping acidified seawater in the reactor, at which point a steady state was reached. After 21 days from starting the experiment, the steady state was assumed to be reached when the pH of the overlying water was unchanged for 3 consecutive days. Measurements done at this timepoint are labeled "RDR1" and include total alkalinity (TA) analysis of a sample of the output solution and three pH microprofiles: at the center of the sediment disk, 3.5 cm from the center and 7 cm from the center near the edge, see Figure A6 in Supporting Information S1. The average pH across these three microprofiles was computed.

Then, a line of 15 evenly spaced aragonite balls (diameter of 1–2 mm) was added from the center to the outer edge of the sediment disk. The pH of the overlying water was once again monitored daily until a steady state was reached after another 27 days. A sample for TA analysis was taken from the output solution and three microprofiles were measured at the center, 3.5 cm from the center and 7 cm from the center along the line of aragonite balls (see Figure A6 in Supporting Information S1 for approximate locations). The average of these three profiles was computed. The second steady state time point is referred to as "RDR2".

To increase the aragonite surface coverage once more, 15 more aragonite balls were added along the same line, see Figure A6 in Supporting Information S1. pH was monitored daily until a steady state was reached after another 16 days. The pH microprofiles and an alkalinity sample were taken at the same locations as at the previous time point, this time labeled “RDR3”.

2.2.3. Dissolution Rate Computation

For each result timepoint (RDR1, RDR2, and RDR3), at steady state, the alkalinity difference (ΔTA) between the input solution (60 L batch of seawater with $\Omega_{ca} = 0.3$) and the output solution was calculated. The dissolution rate r ($\text{mol m}^{-2} \text{yr}^{-1}$) was then calculated using

$$r = \frac{m_{sw} * \Delta TA}{2 * SA * \Delta t}$$

where m_{sw} is the mass of seawater present in the reactor (1.51 ± 0.05 kg), Δt is the residence time of the solution in the reactor (130.2 ± 8.0 hr), as given by the volume of the solution in the reactor divided by the pumping rate, and SA is the surface area of the SWI (176.7 ± 1 cm^2).

2.3. Experiment 2: Cuvette (CUV) Experiment

2.3.1. pH Microprofiling in Cuvettes

Two glass cuvettes ($51 \times 18 \times 57$ mm) were each filled with ~ 14 g of calcite sand (layer thickness of 34 mm) and acidified seawater ($\Omega_{ca} = 0.3$). The “control” cuvette denoted thereafter as “CUV CTRL” contained only calcite sand and seawater, whereas the other cuvette, thereafter “CUV P” also included 260 mg (layer thickness of 1 mm) of homogeneously distributed juvenile pteropods spread over the sediment surface. Starting 15 min after adding the seawater and pteropods (see Figure A2 in Supporting Information S1 for profiling set-up), two pH profiles (with depth steps of 100 μm) per cuvette were measured, always at a different location, every hour for the first day, and then once daily the following 3 days. Four different electrodes were used during these experiments due to successive microsensors breaking, as the tiny sensor tips are fragile. At the end of the experiments, the overlying seawater was sampled for TA analysis. The sediment was scooped out of the cuvettes in depth layers of ~ 3.5 mm-thick, and the retrieved sediment samples were then dried and stored for XRPD analysis. Juvenile pteropods were separated from the sediment for visual inspection under a microscope, and returned to their original samples afterward.

When the standard deviation of any pH_T data point was larger than 0.02, this data point was omitted (3% of 4,262 data points). There were seven resulting profiles for CUV P (with pteropods) and five profiles for CUV CTRL (no pteropods). Unfortunately, the fragility of the microelectrodes caused breakages, so CUV CTRL has fewer profiles than CUV P. See Table A2 in Supporting Information S1 for the elapsed time, electrode used and corresponding calibration slope gradients (all in the range -57.45 to -52.46 mV per pH unit at 20.9°C).

2.3.2. RADI Model

Model simulations aiming to reproduce the pH profiles from cuvette experiments were performed using the RADIV1 one-dimensional sediment porewater model of Sulpis, Humphreys, et al. (2022) in its MATLAB version. This model is targeted for the study of deep-sea calcium carbonates, incorporating both calcite and aragonite dissolution, as well as calcite precipitation. The aim of these simulations was to reproduce the measured pH_T profiles, using TA and dissolved inorganic carbon (DIC) as the only reactive solutes present and calcite and aragonite as the only reactive solids composing the sediment. Initial calcite and aragonite concentrations were set to the values measured by X-ray diffraction, and initial DIC and TA were set to $672 \mu\text{mol kg}^{-1}$ and $681 \mu\text{mol kg}^{-1}$, respectively, to reproduce the observed initial Ω_{ca} . As in the cuvettes, in the model simulations, molecular diffusion was the only mode of solute transport and solid particles were immobile. The calcite and aragonite dissolution rate constants, as well as the calcite precipitation rate constant were then tuned to reproduce the pH profiles. Molecular diffusion was the only mode of transport considered. The porosity and amount of CaCO_3 were assumed to be constant with depth, as supported by our XRPD results discussed later in the Results and interpretation Section 3. Phosphate and silicate concentrations were also included as model variables because they are used to compute pH_T along with TA and DIC, but they were assumed to be non-reactive. The depth

resolution of the model was set to 500 μm , and the time steps taken by the model were about 60 s. A link to the model code is provided in the 'Data Availability Statement' section, and a complete overview of all model parameters is provided in Table A3 in Supporting Information S1.

2.3.3. Assumptions

For our analysis of the cuvette experiments and model, several assumptions were made: (a) chemical gradients were assumed to be laterally homogenous, (b) no precision or accuracy difference between the different electrodes used, (c) the water above the sediments was assumed to be both vertically and laterally homogenous due to Brownian motion, and mixing caused by the inserting and removing of the micro- and reference electrodes, (d) constant laboratory air $p\text{CO}_2$, and (e) negligible respiration occurring within the sediment (see Figure A1 in Supporting Information S1).

2.4. Analytical Techniques

2.4.1. pH Microelectrodes

To obtain insight into micro-scale pH changes, we used microelectrodes to measure pH. They have a high spatial resolution, do not significantly damage the sample being measured, achieve high rates of diffusion (hence fast responses to change) and suffer much less from ohmic and double layer charging distortions than larger electrodes (Štulík et al., 2000). The pH microelectrodes used in this study (Unisense A/S, Aarhus, Denmark) have tip diameters of 100 microns and an external reference electrode (Ag-AgCl). The electrodes were calibrated against three Certipur buffer solutions with NBS/NIST-scale pH of 4.00, 7.00, and 10.00 at 20°C. A linear regression of the electrode response to these buffers was used to obtain the Nernstian slope. Measurements were converted to the total hydrogen ion concentration scale by altering the y-intercept of the calibration curve using a self-made 2-amino-2-hydroxymethyl-1,3-propanediol (tris) buffer with a pH_T of 8.097 ± 0.000 at 25°C, as described by Paulsen and Dickson (2020). This meant a pH_T of 8.223 ± 0.007 at 20.9°C (DeValls & Dickson, 1998). Note that all pH values in this paper are reported on the total hydrogen ion scale (pH_T) (Zeebe & Wolf-Gladrow, 2001). The temperature dependency of the Nernst equation, and thus the temperature dependency of the theoretical slope of a pH sensor, is compensated for by the Unisense software when calibrating the electrodes. Unisense states that any linear slope of 50–70 mV/pH unit is acceptable. See Table A2 in Supporting Information S1 for the calibration slopes and the y-intercepts. After calibration, vertical profiling was done using a Unisense high-precision micromanipulator (μm scale).

2.4.2. Alkalinity Measurement

Initial alkalinity measurements of seawater were carried out at the NIOZ Royal Netherlands Institute for Sea Research by potentiometric titration using a Versatile INstrument for the Determination of Titration Alkalinity (VINDTA) 3C (Marianda, Kiel), while remaining alkalinity measurements were analyzed spectrophotometrically on a Seal QuAAtro due to smaller sample volumes, following Sarazin et al. (1999). TA was computed from potentiometric titration data using the Python package Calculate v23.3 (Humphreys & Matthews, 2022). All TA measurements were calibrated using batch #186 certified reference material (CRM) seawater obtained from A.G. Dickson (Scripps Institute of Oceanography, USA). Samples were also analyzed for salinity (WTW Multi 340i), which was assumed to remain constant for the remainder of the experiments. Experiments were carried out at the Utrecht University Geolab ($T = 20.9^\circ\text{C}$ and $p\text{CO}_2 \approx 480$ ppm, measured using a Claire PTH-5 meter with NDIR sensor).

2.4.3. CO₂ System Calculations

PyCO2SYS v1.8.0 (Humphreys et al., 2022), originating from the algorithm by Lewis and Wallace (1998), was used to solve the carbonate system and propagate uncertainties. The same "standard" uncertainties for the equilibrium constants and total borate were used as in CO2SYS for MATLAB (Orr et al., 2018). The equilibrium constant parameterizations used to model carbonic acid dissociation were taken from Lueker et al. (2000), as recommended by best practises (Dickson et al., 2007). The dissociation constant for bisulfate was taken from Dickson (1990), for fluoride from Dickson and Riley (1979), and total borate was calculated from salinity following Uppström (1974).

2.4.4. X-Ray Powder Diffraction

Each sample was prepared for quantitative X-Ray Powder Diffraction (XRPD) by McCrone milling for 5 min in 10 mL 2-Propanol. Each sample was spiked with approximately 10 wt% corundum, and the weights were recorded precisely. The spiked samples were homogenized by dry McCrone milling for 1 min. Spiked sample powders were backloaded onto polymethyl methacrylate (PMMA) sample holders with a cavity diameter of 25 mm. The samples were run at the Department of Earth Sciences of Utrecht University on a Bruker D8 Advance with a LYNXEYE detector and a θ/θ goniometer. Cu- $K\alpha$ radiation ($\lambda = 1.54056 \text{ \AA}$) was used and the tube was operated at 40 kV and 40 mA. To obtain quantitative results, a primary Soller slit of 4.1° , as fixed divergence slit (0.165 mm)—resulting in a constant irradiated volume, and a motorized anti-scatter screen were used. XRPD patterns were recorded from 3 to $80^\circ 2\theta$, in 0.02° steps, and counting for 0.85 s per step. Samples were spun continuously during measurement (0.25 Hz).

An in-house reference library of standard XRPD patterns of pure minerals was used. This library was compiled from specimens of pure minerals obtained from various mineral collections. All standard XRPD patterns were scaled to a maximum intensity of 1,000 counts prior to determination of a full-pattern reference intensity ratio (RIR) from a mixture of the pure mineral with corundum as an added internal standard, for which the weight fractions were known precisely. All standard XRPD patterns were run under the same diffractometer conditions as the unknown samples. Quantification of the mineral phases in the unknown samples was carried out using the full pattern summation methodology implemented in the package *powdR* for the R Language and Environment for Statistical Computing (Butler & Hillier, 2021).

3. Results and Interpretations

3.1. Experiment 1: Rotating Disk Reactor

The first experiment aimed at quantifying how the total CaCO_3 dissolution-generated alkalinity flux through the SWI changes when various amounts of aragonite are added onto a calcite seabed by measuring bulk seawater TA and pH porewater profiles, under hydrodynamic conditions representative of benthic environments.

After 21 days of experiment in which a calcite sand sediment disk was dissolving in acidified seawater, the pH of the overlying waters reached a steady state (timepoint RDR1). At that point, the pH decrease caused by the injection of acidified water into the reactor chamber was balanced by the pH increase caused by CaCO_3 dissolution. At RDR1, microprofiles indicated a sharp pH increase with depth in the top 5 mm of the calcite sand (Figure 2), and stable pH values deeper in the porewaters. In terms of $[\text{H}^+]$ (Figure 2; note inverted x-axis), it translates into a $44 \pm 2 \text{ nM}$ (32%) decrease within the top 5 mm of the sediment relative to the average overlying water $[\text{H}^+]$ ($65 \pm 2 \text{ nM}$), as H^+ is consumed by the calcite dissolution reaction (Figure 2). The whole pH profile at RDR1 is below the baseline, that is, the pH of the acidified water initially poured within the reactor chamber. This could partly be due to microbial respiration occurring within the sediment. After 27 days, following the addition of 15 aragonite balls onto the calcite sand surface (Figure A6 in Supporting Information S1), at steady state (RDR2), pH increased (and $[\text{H}^+]$ decreased) in the porewaters and in the overlying waters relative to RDR1. The shape of the pH and $[\text{H}^+]$ profiles remained the same, but the pH increase ($[\text{H}^+]$ decrease) in the top sediment layer was smoother, occurring over the sediment top centimeter. After the addition of 15 more aragonite balls and another 16 days, at steady state (RDR3), pH increased (and $[\text{H}^+]$ decreased) slightly relative to RDR2. For RDR2 and RDR3, porewater $[\text{H}^+]$ was as much as $15 \pm 0.5 \text{ nM}$ and $16 \pm 0.5 \text{ nM}$ smaller than their average overlying waters value, respectively. The H^+ consumption in the sediment porewaters, relative to the overlying waters, was much smaller in RDR2 and RDR3 when compared to the pure calcite sediment in RDR1. This is attributed to an increase by up to 0.4 mol kg^{-1} in buffering capacity (β_{Alk} , a measure of the resistance to change of H^+ concentration when TA changes at constant DIC, as explained by Egleston et al. (2010)), computed using PyCO2SYS v1.8.0 (Humphreys et al., 2022).

As aragonite balls were successively added onto the calcite sediment surface, overlying-water saturation state with respect to calcite and aragonite and calcite increased (Table 2, Figure 3). The degree of undersaturation ($1 - \Omega$) for both calcite and aragonite was plotted against the computed CaCO_3 dissolution rate (Figure 3). The three computed dissolution rates ranged from 79 to $102 \mu\text{mol m}^{-2} \text{ hr}^{-1}$ and were statistically undistinguishable from each other, that is, they did not increase throughout the course of the experiment as aragonite was added. The computed dissolution rate corresponds to an alkalinity flux out of the sediment disk, and accounts for the net

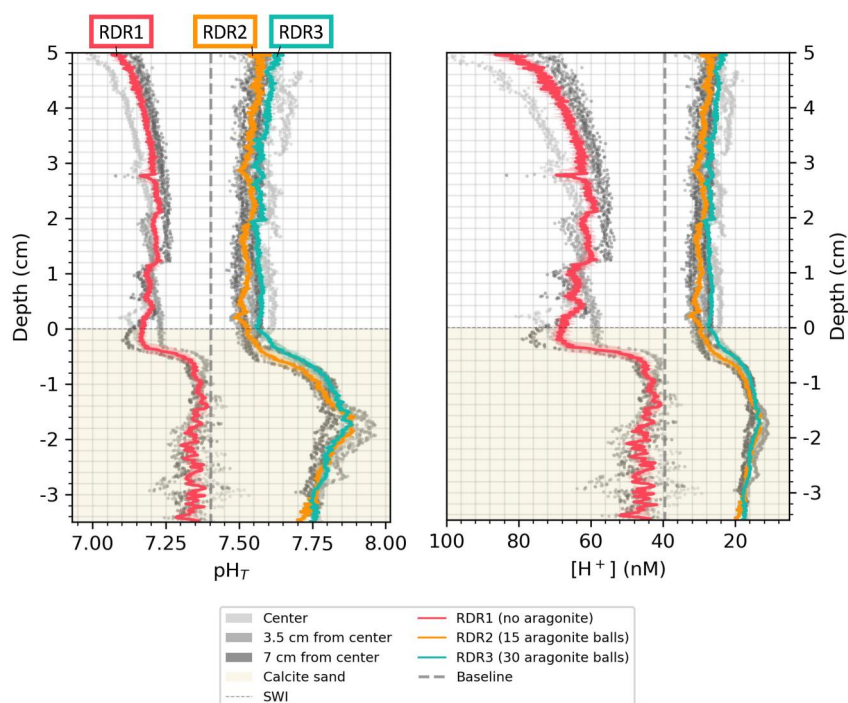


Figure 2. Rotating disk reactor profiles. Left shows pH_T and right shows $[\text{H}^+]$ (note inverted x -axis). Uncertainties of the mean profiles shown by shading: depth uncertainty of 0.1 cm, uncertainty consists of microelectrode and tris standard deviations. For RDR and RDR3, the data at 3.5 and 7 cm from the disk center cannot easily be seen because it is behind the colored curves, indistinguishable from the data gathered at the disk's center.

dissolution rates of all calcium carbonate phases present. Thus, a possible interpretation for this unchanged dissolution rate could be that calcite and aragonite dissolution rates are evolving in opposite directions.

When normalized by the SWI-surface area, the computed dissolution rate of a pure calcite sediment disk is close to that predicted by classic, calcite dissolution rate laws (Figure 3). Addition of aragonite should cause a rise in the dissolution rate. If the sediment disk was made of pure aragonite, the computed dissolution rate would be higher, in agreement with previously published aragonite dissolution rate laws (Figure 3). Without any buffering effect, a sediment disk that is partly made of calcite and partly made of aragonite should emit a net alkalinity flux that is in between the predicted aragonite and calcite dissolution rates.

In reality, because the addition of aragonite buffers the surrounding waters and raises saturation states, calcite dissolution rate decreases as aragonite dissolution rate increases. Throughout the course of our experiment, because the total (net) CaCO_3 dissolution rate was unchanged, we hypothesize that the aragonite dissolution rate increase caused a calcite dissolution rate decrease of the same value.

Table 2
Rotating Disk Reactor ΔTA , Average pH_T and Saturation States^a

	ΔTA ($\mu\text{mol kg}^{-1}$)	Average pH_T water column	Ω_{ca} overlying water	Ω_{ar} overlying water
RDR1	972.941 ± 5.4	7.188 ± 0.015	0.287 ± 0.019	0.183 ± 0.012
RDR2	942.451 ± 5.4	7.537 ± 0.015	0.593 ± 0.039	0.380 ± 0.025
RDR3	966.961 ± 5.4	7.580 ± 0.014	0.668 ± 0.043	0.428 ± 0.028

^aFor each timepoint during the RDR experiment, shows ΔTA of output water (collected after steady state was reached and pH_T profiles were done) relative to the TA of the input seawater ($\Omega_{\text{ca}} = 0.3$), the average pH_T measured in the water column by the microelectrodes and the computed Ω_{ca} of the overlying water for $T = 20.9^\circ\text{C}$ and $S = 28.3$. Uncertainties for TA originate from VINDTA and QuAAtro and pH_T uncertainties from microelectrode and tris standard deviations. These uncertainties together with a temperature uncertainty of $\pm 0.05^\circ\text{C}$ as well as the aforementioned “standard” uncertainties were used to compute Ω uncertainties in PyCO2SYS v1.8.0 (Humphreys et al., 2022).

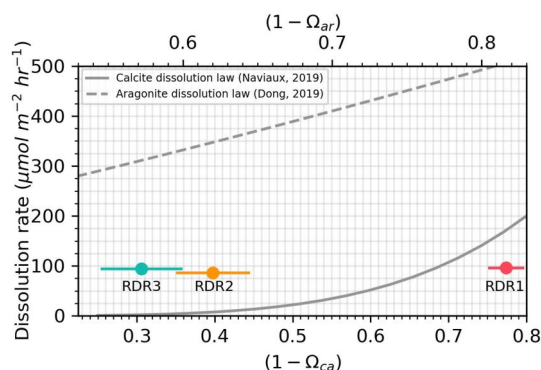


Figure 3. The dissolution rate (calculated using ΔTA) plotted against the degree of undersaturation ($1 - \Omega_{ca}$). Uncertainty propagation of the dissolution rate computed with $m_{sw} \pm 0.05$ kg, $\Delta TA \pm 5.4$ $\mu\text{mol kg}^{-1}$ (from QuAAtro), $SA \pm 1 \times 10^{-4}$ m^2 and $\Delta t \pm 8$ hr. Calcite saturation state uncertainty computed based on $TA \pm 5.4$ $\mu\text{mol kg}^{-1}$, $\text{pH}_T \pm 0.015$ (based on the average standard deviations given by the Unisense software and the standard deviation of tris) and $T \pm 0.05^\circ\text{C}$. Dissolution rate law for calcite was taken from Naviaux et al. (2019) and dissolution rate law for aragonite from Dong et al. (2019).

3.2. Experiment 2: Cuvette Experiment

The second experiment consisted of dissolving (aragonite) pteropod shells on calcite sand in a smaller setting: a quartz glass cuvette filled with undersaturated, natural seawater in the absence of flow. The goal was to measure the effects of aragonite dissolution on porewater pH profiles at a high spatial and temporal resolution, and to use these results in combination with a diagenetic model to quantify the calcite and aragonite dissolution rates, as well as the calcite precipitation rate. The dissolution experiment was carried out in two experimental cuvettes, one containing a layer of pteropod shells on top a calcite sand bed (CUV P), another one simply containing calcite sand (CUV CTRL). Thereafter, “elapsed time” refers to the amount of time that has passed since the addition of the pteropod layer in CUV P.

3.2.1. pH Microelectrode Profiles

In both cuvettes, in the overlying waters and in the porewater, pH showed a marked increase within the first hour, and for the rest of the experiment, was consistently higher than the baseline pH (and $[\text{H}^+]$ was lower than the baseline, Figure 4). After 1 hour, in both cuvettes, $[\text{H}^+]$ concentration slowly decreased with depth within the overlying waters, at a rate of 10 nmol cm^{-1} in CUV P and 2.6 nmol cm^{-1} in CUV CTRL. In both cuvettes, the largest

decrease in $[\text{H}^+]$ occurred in the porewaters, just below the SWI. At both 1 and 2 hr, $[\text{H}^+]$ decreased by a maximum of 10.8 nM compared to $[\text{H}^+]$ at the top of the water column in CUV P, whereas $[\text{H}^+]$ decreased by 7.7 nM in CUV CTRL. Deeper in the porewaters, at about 2 mm below the SWI, $[\text{H}^+]$ increased again with depth in CUV P, but was stable in CUV CTRL.

After 4 hours, the pH maximum at the SWI was no longer as pronounced in CUV P and CUV CTRL reached a maximum pH_T within the water column of 7.60. Relative to the baseline pH of 7.40, 79% of the H^+ ions originally in CUV P had been consumed within 4 hr, whilst in CUV CTRL only 37% of H^+ ions were consumed. Thus, the presence of pteropods doubled the amount of H^+ ions consumed after 4 hr. Within the overlying waters, CUV P reached a minimum $[\text{H}^+]$ of 8.2 nM (pH_T of 8.08) at 7 hr, compared to a minimum of 19.3 nM at 4 hr in CUV CTRL (note that there is no profile at 7 hr for CUV CTRL).

In CUV CTRL, between an elapsed time of 7 and 25 hr, pH profiles did not show any obvious change. In CUV P, however, porewater pH started decreasing between 7 and 25 hr, with a maximum decrease at around 5 mm below the SWI, below the pteropod layer, and kept decreasing at 50 and 72 hr, eventually getting back to the baseline level. This suggests that in CUV P, the maximum rate of dissolution was reached between 7 and 25 hr, after which another process started dominating the pH signal, leading it to decrease.

3.2.2. Overlying Waters' Chemistry

Relative to the initial TA of the $\Omega_{ca} = 0.3$ seawater, the TA of CUV P increased by 2089 ± 5.4 $\mu\text{mol kg}^{-1}$ and that of CUV CTRL increased by 845 ± 5.4 $\mu\text{mol kg}^{-1}$ (Table A1 in Supporting Information S1). Thus, by difference, the minimum alkalinity addition that is due to pteropod shells dissolution is 1244 $\mu\text{mol kg}^{-1}$. Assuming that this alkalinity was homogeneously mixed within all the water in the cuvette, this would represent about 25 μmol of alkalinity released by aragonite dissolution, that is, 1.2 mg of aragonite dissolved. For comparison, 260 mg of aragonitic pteropod shells were initially placed in CUV P.

The final saturation states of the overlying seawater of both cuvettes were calculated using TA (of the overlying seawater after the last profile) and the average pH in the water column of the final run. This resulted in final $\Omega_{ca} = 1.83 \pm 0.22$ and $\Omega_{ar} = 1.17 \pm 0.14$ for CUV P, and $\Omega_{ca} = 1.09 \pm 0.02$ and $\Omega_{ar} = 0.70 \pm 0.05$ for CUV CTRL (at $T = 20.9^\circ\text{C}$ and $S = 28.3$).

The presence of aragonite in CUV P allows the seawater to become supersaturated with respect to calcite ($\Omega_{ca} = 1.83 \pm 0.22$). Thus, a reason for the large pH decline seen in CUV P could be reprecipitation of calcite within pores of the sediment, explaining the lowering of pH seen in CUV P. The ‘halo’ of supersaturation caused

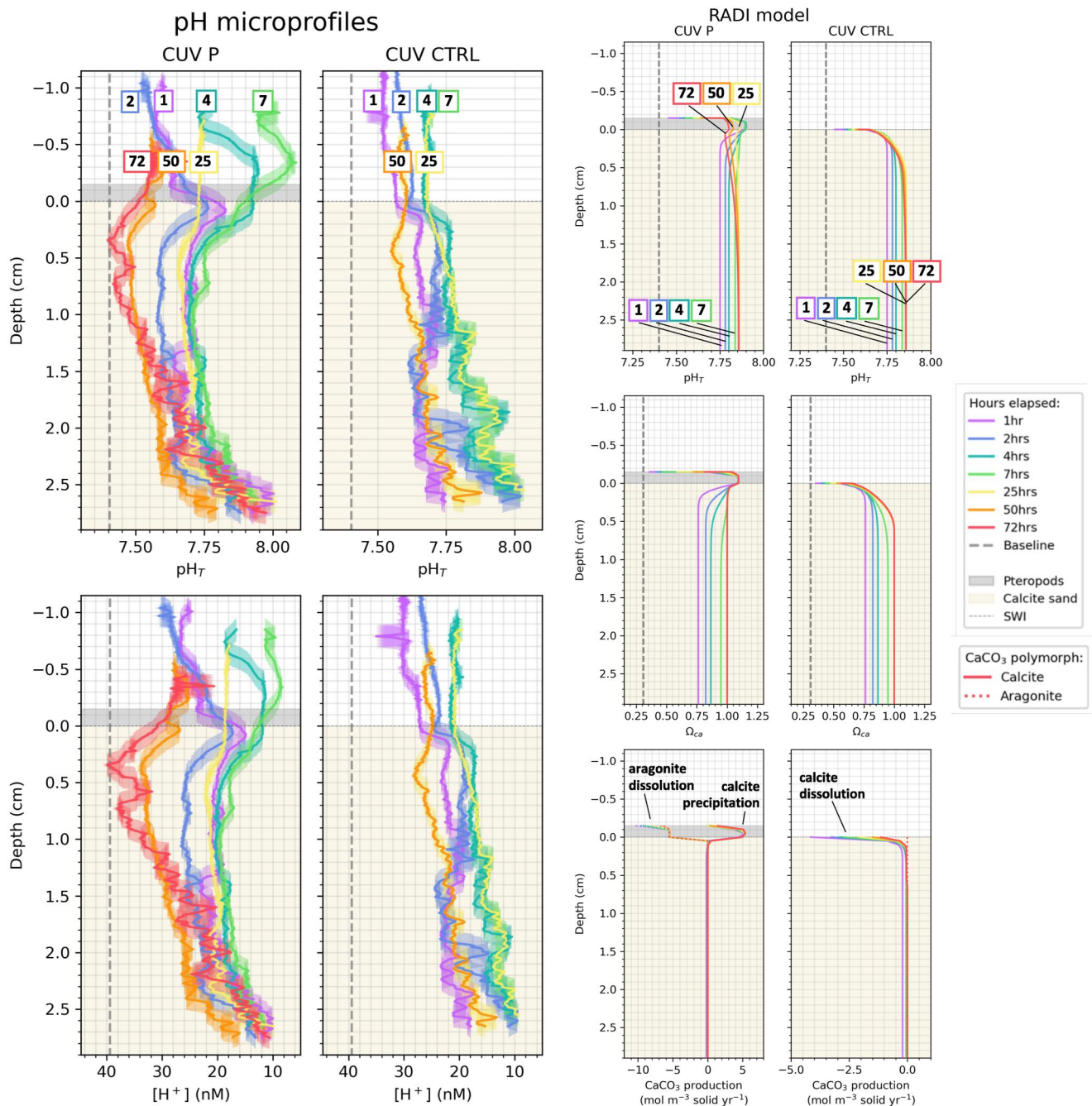


Figure 4. Left: plots of the average of each consecutive pair of pH_T profiles in CUV P (with pteropod layer) and CUV CTRL (without pteropod layer) against depth, over time, as well as [H⁺] against depth over time. The vertical gray dashed line shows the baseline: the pH_T of the seawater (7.40) before adding it to the cuvette. Errors are indicated by the shaded areas. The x-error is equal to the standard deviation of microelectrode pH_T measurements, but is much smaller than the line width (average std dev = 0.0038) as data points with a SD > 0.02 have been omitted. There is a y-error of ±1 mm caused by manual alteration of depths per profile when switching electrodes due to different electrode lengths, as well as an uneven sediment surface. Note SWI in CUV P refers to the start of the calcite sand, not pteropods. Right: RADIv1 model (Sulpis, Humphreys, et al., 2022) results. Input parameters shown in Table A3 in Supporting Information S1 and reaction rates shown above. Calcite production is shown by the solid lines, aragonite production by the dashed lines. Depth resolution was 0.5 mm steps. Note that calcium carbonate production rate is given in mol per m³ of solid (all solids, excluding porewater) per year, hence, negative values represent dissolution. Numbers in colored squares correspond to the elapsed time for each pH or [H⁺] profile.

by pteropod dissolution may not have been felt as strongly below 0.5 cm depth, explaining why pH increased again below this depth.

The saturation of CaCO_3 is sensitive to both DIC and TA, and this effect was quantified by computing buffer factors using PyCO2SYS v1.8.0 (Humphreys et al., 2022). The ω_{DIC} buffer factor was used to quantify the capacity to buffer changes in Ω as DIC increases and TA remains constant, and the ω_{TA} for the buffering capacity of Ω as TA increases and DIC remains constant (Egleston et al., 2010). Relative to the initial seawater, ω_{DIC} increased by 5.40 for both CUV P and CUV CTRL, indicating aragonite had no effect. However, ω_{TA} decreased by 4.94 for CUV P and increased by 4.51 for CUV CTRL. This shows how the dissolution of aragonite reduces the seawater's ability to resist changes in Ω , making it more sensitive to changes in carbonate chemistry.

In CUV P, the overlying waters end up slightly supersaturated with respect to aragonite. This could also have been due to the presence of an even more soluble CaCO_3 polymorph, such as vaterite (undetected in XRPD results, but may have been present in small amounts), or a short-lived surface phase that develops upon the introduction of the pure calcite to the seawater solution, as previously shown with magnesium calcite by Mucci and Morse (1984).

A lid was put on the cuvette (not air-tight) in between measurements to prevent evaporation, as an increase in salinity could lead to an underestimation of the TA and saturation states. It should be noted some water loss was visible in both cuvettes (also shown in Figure 4 by the lower start of the profiles over time), most likely caused by the reference electrode moving in and out of the cuvettes. This effect was especially noticeable in CUV P, which may have amplified the effect of pteropod dissolution on TA relative to CUV CTRL. Taking the lid on and off could also have affected pH: when the lid is on, pH goes up due to calcite dissolution and CO_2 neutralization, but when the lid is taken off, more rapid re-equilibration with the air could occur and allow more CO_2 to be taken up and pH to decrease.

3.2.3. Visual Changes

A Keyence VHX-7000 digital microscope was used to observe the pteropods and calcite sand before and after dissolution (Figure A3 in Supporting Information S1). At the end of the experiments, the pteropod shells had remained structurally intact. Before the experiment they had fully translucent shells with no discernible areas of dissolution. After dissolution, the protoconch was opaquer with a milkier color and rougher texture (Figure A3 in Supporting Information S1). The same observations were made by Johnson et al. (2016) when dissolving juvenile pteropods. There are no visual differences observed when comparing calcite sand (foraminiferal ooze) in CUV P and CUV CTRL. Other studies have observed calcite recrystallization on the surface of foraminifera, attributed to the calcite supersaturation surrounding dissolved aragonite particles at the seafloor (Collen & Burgess, 1979; Pearson et al., 2015), but this was not visible for our experiments under the microscope.

3.2.4. XRPD

XRPD results (Table A4 in Supporting Information S1) for CUV P showed that in addition to calcite (77%) and halite (5%), aragonite (14%) and quartz (5%) were only present in the top 3.5 mm layer. In CUV CTRL, no aragonite and only negligible amounts of quartz were found throughout all the inspected layers. The percentage of calcite ranged between 97% and 98% in CUV CTRL and did not show any particular depth variation, as Ω_{ca} was around 1 throughout the entire cuvette. The percentage of halite did not vary by more than 1% in either cuvette when excluding the top layer. Unfortunately, the XRPD results cannot prove whether the supersaturation caused by pteropod dissolution actually suppressed calcite dissolution. This is because the change in the amount of calcite dissolved was too small to measure.

3.2.5. RADI Model

The model input parameters used to fit pH profiles from both cuvettes are given in Table A3 in Supporting Information S1, with TA, DIC, calcite and aragonite used to solve for the CO_2 system (phosphate and silicate concentrations were also used but are assumed constant). The conditions for both CUV P and CTRL were the same, except for the mask function used to create a pteropod layer of 0.15 cm in CUV P. This pteropod layer consisted of 48% aragonite, with the remaining 52% consisting of calcite and quartz (estimation based on the XRPD results shown in Table A4 in Supporting Information S1). The top boundary condition was a DBL control at the SWI, as explained by Sulpis, Humphreys, et al. (2022). The DBL was assigned a depth of 1 mm, as this

Table 3
RADI Model Reaction Rates, With Rate Constants Tuned According to Cuvette Experiment Results

	Rate	For:	Rate order taken from:
Aragonite dissolution	$0.0166\% \text{ day}^{-1} * [\text{Aragonite}] * (1 - \Omega_{\text{ar}})^{0.13}$ $0.18\% \text{ day}^{-1} * [\text{Aragonite}] * (1 - \Omega_{\text{ar}})^{1.46}$	for $\Omega_{\text{ar}} > 0.835$ for $\Omega_{\text{ar}} \leq 0.835$	Dong et al. (2019)
Calcite dissolution	$1.7 * 10^{-4}\% \text{ day}^{-1} * [\text{Calcite}] * (1 - \Omega_{\text{ca}})^{0.11}$ $0.54\% \text{ day}^{-1} * [\text{Calcite}] * (1 - \Omega_{\text{ca}})^{4.7}$	for $\Omega_{\text{ca}} > 0.8275$ for $\Omega_{\text{ca}} \leq 0.8275$	Naviaux et al. (2019)
Calcite precipitation	$411 \text{ mol} * (\text{m}^3 * \text{day})^{-1} * [\text{Calcite}] * (1 - \Omega_{\text{ca}})^{1.76}$	for $\Omega_{\text{ca}} > 1$	Zuddas and Mucci (1998)

allowed reproduction of the smooth shape of the microprofiles. The overlying water seemed well-mixed throughout the cuvette experiments as evidenced by lack of gradients, so was assumed mixed and thus constant in the model. CO₂ exchange was parameterized in between the water column and the air assuming a constant pCO₂ in the air of 480 ppm, which was measured throughout the cuvette experiments in the lab using the Claire PTH-5 meter. Note that the water column was assumed to be at equilibrium with the air, ignoring the presence of the lid used during the experiments. A zero-gradient bottom boundary condition was used for the sediment. Constant porosity was assumed, though this may oversimplify dissolution behavior as porosity gradients affect diffusion rates and thus concentration gradients. The rate constants were manually tuned to fit the model to the experimental results, giving the pH_T and saturation state profiles shown in Figure 4. First, the calcite dissolution rate constant was tuned to reproduce pH profiles in the cuvette with pure calcite. Second, the aragonite dissolution rate constant was tuned to reproduce the shallow, strong pH increase seen in the cuvette with aragonite. Then, calcite precipitation was enabled, and its rate was tuned to reproduce the pH decrease that can be observed in the cuvette with aragonite after the first day of experiments. The reaction rates are given below in Table 3.

The model predicts increasing pH_T and saturation states within the overlying waters over time in both cuvettes (Figure 4). At the bottom of the sediment column, saturation states converge to $\Omega_{\text{ca}} = 1$ in the sediment of both cuvettes. In CUV P, within the pteropod layer, Ω_{ca} reaches a value of 1.1, due to the higher solubility of aragonite. After 7 hr, pH decreases in the sediment up to 1.5 cm depth in CUV P, as seen in the experimental results. This could only be modeled when increasing the calcite precipitation rate, assuming no respiration took place near the SWI. In CUV CTRL, calcite dissolves most within the upper 0.1 cm of the sediment and after 7 hr remains stable below this depth. In CUV P, aragonite dissolves within the pteropod layer and allows calcite to precipitate due to the saturation state (Ω_{ca}) being larger than 1. Just below the pteropod layer this effect is also visible. The production rate was plotted against the degree of undersaturation (Figure A4 in Supporting Information S1) to show this was the same for each run, validating the model output.

The small decline in pH seen within the CUV CTRL during the experiment cannot be explained by the model, seeing as the saturation state will always stabilize at $\Omega_{\text{ca}} = 1$ in the model. This suggests factors out of the scope of this model are at play, such as inhibitors of calcite dissolution/precipitation. Organic matter may exert control by adsorbing to calcite and aragonite surfaces (Carter, 1978), though our understanding of this is limited. Trace metals (e.g., Ni, Cu, Mn, or Co) (Gutjahr et al., 1996), strontium (Lorens, 1981) and especially phosphate (Burton & Walter, 1990; Millero et al., 2001) are also known to influence calcite dissolution by blocking of active sites, with their effectiveness being dependent on saturation state.

Many past studies have invoked inhibitors to explain laboratory-measured dissolution rates (Bischoff et al., 1987; de Kanel & Morse, 1978; Keir, 1980) being faster than those measured in situ (Berelson et al., 1994; Berger, 1967; Fukuhara et al., 2008; Honjo & Erez, 1978; Milliman, 1975; Peterson, 1966). More recent studies have found CaCO₃ dissolution rates in the lab and field to be consistent, especially in the presence of DOC (Dong et al., 2019; Naviaux et al., 2019). The rate expressions used here were found by tuning the calcite and aragonite dissolution rate constants in RADI to match our pH profiles from the lab. Sulpis, Humphreys, et al. (2022) tuned their rate constants to best fit in situ porewater and sediment measurements. These in situ rate expressions were plotted along our rate expressions in Figure A5 in Supporting Information S1. This shows the calcite dissolution rate to actually be slower in the lab than in situ, though both aragonite dissolution and calcite precipitation were faster in the lab. Assuming inhibitors affect both calcite and aragonite equally, this suggests they are unlikely to play an important role in our study.

This diagenetic model and the finite element model built by Sulpis, Humphreys, et al. (2022) simulating the dissolution of a pteropod on a bed of calcite show porewaters reach equilibrium with respect to calcite at approximately 1.5 cm depth. In general, the microelectrode profiles showed pH stabilizing below 0.5 cm depth, and then below 1–1.5 cm pH started to fluctuate. These small fluctuations were probably due to lateral movement of the electrode caused by the compact sediment.

Overall, by reproducing the observed pH profiles, the RAD1 model predicts that up to $5 \text{ mol m}^{-3} \text{ yr}^{-1}$ calcite is produced within the pteropod layer, which for the top $\sim 2.7 \text{ cm}^3$ collected for XRPD analysis and the timespan of the experiment (72 hr) equates to roughly 0.01 mg precipitated calcite. This quantity of calcite would be below the XRPD detection limit and, if precipitation occurred homogeneously over the sediment volume, likely undetectable by imaging techniques (e.g., electron microprobe).

4. Discussion

4.1. The Role of Aragonite in the Calcite Lysocline

In the open ocean, CaCO_3 minerals usually constitute most of the sediments on topographic highs, accounting for 75%–100% of the sediment dry weight over most of the mid-Atlantic ridge (Archer, 1996; Goff et al., 2008). Most sediment composition databases do not include information regarding the mineralogy of the CaCO_3 minerals present, as their concentration is often determined by dissolving all inorganic carbon with an acid, rather than identifying minerals with X-ray diffraction or Raman spectroscopy (Ellis & Moore, 1973; Hülsemann, 1966; Turekian, 1956). In addition, the sampling of sediments from the deep seafloor using classical coring techniques can take a few hours before sediments are retrieved and stored on board, a time during which soluble carbonate minerals such as in pteropod shells or fish–gut carbonate secretions could be altered or dissolved, thus biasing any mineralogical data that is not collected and stored in situ. As a result, global maps of aragonite and calcite sediment contents are unavailable, although some scattered aragonite sediment content estimates can be found in the literature (Berger, 1978).

Our results suggest that as long as aragonite is present and dissolving in a calcite-containing sediment, the alkalinity flux released by total CaCO_3 dissolution should not be affected by saturation state changes. While the addition of aragonite brings the total CaCO_3 dissolution rate up, its buffering effect brings the calcite dissolution rate down, so that the net total CaCO_3 dissolution rate change is unnoticeable within the uncertainty of alkalinity fluxes (Figure 3). This may have important implications for our interpretation of the calcite lysocline, the depth range over which the calcite content in sediments decreases significantly and that would be, at steady state, located between the calcite saturation depth and the calcite compensation depth (Boudreau et al., 2018). Some authors have, instead, argued that the calcite lysocline starts deeper than the calcite saturation depth, because of the slow calcite dissolution rates near equilibrium (Adkins et al., 2021; Subhas et al., 2015). We suggest that this interpretation can be further complicated by the presence of aragonite, and that the upper limit of the calcite lysocline may correspond to the depth below which aragonite does not accumulate in the sediments.

As the aragonite flux to or residence time at the SWI decreases with water depth, its buffering effect should diminish and, eventually, below a critical depth, disappear. Below this critical depth, as there is no aragonite to dissolve, calcite dissolution should increase – and the calcite content decrease – with water depth, that is, the calcite lysocline starts. In reality, because there are also many different types of Mg-rich calcites produced in the ocean (Chave, 1954; Wilson et al., 2005), most of them with a solubility higher than that of aragonite (Mackenzie et al., 1983; Reeder, 1983), aragonite would also be protected against dissolution by those more soluble carbonate minerals above the aragonite lysocline. This study highlights the need to consider more soluble carbonate phases when interpreting the depth distribution of a given carbonate mineral, in the present day, in paleo-records and for future predictions.

4.2. Past and Future Carbonate Sediments Burnout

Many events of widespread CaCO_3 seafloor dissolution have been documented from the geological record. In sedimentary rock outcrops these events are characterized by the transition from a CaCO_3 -rich to a CaCO_3 -poor layer, for example, in limestone–marl alternations, although other diagenetic factors can play a role (Westphal, 2006). Such events are often attributed to the spreading of acidified waters along the seafloor, following massive CO_2 emissions due to volcanic eruptions, the release of methane from cold seeps, or the burning of fossil

fuels (e.g., Haynes & Hönisch, 2020; Sulpis et al., 2018; Zachos et al., 2005). An additional explanation could be that the calcite preserved in those sediments dissolved once aragonite stopped accumulating because of other factors linked to evolving surface-ocean ecosystems. Pelagic aragonite producers are ubiquitous and diverse today, mostly represented by pteropods and heteropods, but also in the past, represented for instance by ammonoids (Buchardt & Weiner, 1981; Peijnenburg et al., 2020; Wall-Palmer et al., 2020). Those groups may evolve through time, eventually reducing or dropping their shells (Lalli & Gilmer, 1989), or may simply migrate in response to environmental or ecosystem changes (Comeau et al., 2012; Johnson & Hofmann, 2020; Orr et al., 2005). If aragonite does not accumulate at a given location at the seafloor, the onset of calcite dissolution may be triggered. This could explain regional differences in the paleo-acidification record, because aragonite producers may have been affected by climatic, evolutionary, or ecosystem changes differently depending on the location.

Aragonite-producing organisms are among the first responders to the current ocean acidification episode, with aragonite often seen as a predictor for the future effects of ocean acidification (Gardner et al., 2018). The oceanic uptake of anthropogenic CO₂ has already resulted in the shoaling of the aragonite saturation horizon by 40–200 m over the past century in various oceanic basins (Feely et al., 2004). One of the first and most severely affected regions by ocean acidification is the Southern Ocean, of which 70% is predicted to be undersaturated in aragonite by 2,100 (Hauri et al., 2015). This means that the Southern Ocean seafloor, in particular, could receive less aragonite thus have a weakening of the aragonite buffering effect. This buffering effect mainly occurs in areas of the seafloor where calcite is abundant and dissolving, that is, below the calcite saturation depth and above the calcite compensation depth (Morse & Mackenzie, 1990). This currently represents about 40% of the seafloor (Sulpis, Agrawal, et al., 2022). However, shoaling of the calcite saturation horizon will mean areas where this is currently taking place may no longer be above the calcite compensation depth, whilst areas currently situated above the saturation horizon may become new areas of aragonite buffering.

In shallow carbonate platforms, recent research has reported the presence of non-skeletal aragonite muds resulting from abiotic precipitation (Geyman et al., 2022), which may also facilitate the preservation of other carbonate grains. Upon rising pCO₂, shallow carbonate factories may precipitate less aragonite, which would be an almost immediate CO₂ sink, and act as a negative feedback mechanism (Geyman et al., 2022). Our results suggest that this negative feedback could be enhanced by the CaCO₃ dissolution triggered by the fewer aragonite muds.

4.3. Dynamic Equilibrium and Calcite Overgrowths

In addition to the buffering effect provided by aragonite dissolution, the model simulations suggest that calcite precipitation could be occurring within the sediment. It is possible that calcite overgrowths develop on the surface of calcitic foraminiferal grains, as observed in deep-sea sedimentary foraminifera samples (Collen & Burgess, 1979; Hover et al., 2001). Other carbonate minerals, such as manganese carbonates, have been observed as precipitates on sedimentary foraminiferal surfaces (Boyle, 1983). Calcite precipitation triggered by aragonite dissolution may also contribute to preserving relics of sedimentary aragonite structures, such as skeletons of nautilids or ammonites, via the precipitation of molds (Bruni & Wenk, 1985; Janiszewska et al., 2018; Palmer & Wilson, 2004). As aragonite dissolves, dissolution products simultaneously recrystallize into more stable phases, constituting a multiphase dynamic equilibrium.

4.4. Recommendations for Future Research

A major caveat in our understanding of marine aragonite cycling is the complete absence of agreement regarding its production rate at the ocean surface at the global scale (Bednaršek et al., 2012; Berner, 1977; Buitenhuis et al., 2019; Gangstø et al., 2008). On the regional scale, in the North Pacific gyre, recent research reported that pteropods and heteropods contribute ~14% and ~1%, respectively, to the CaCO₃ standing stock, in the form of aragonite (Ziveri et al., 2023), much lower than along the coasts in the same basin (Buitenhuis et al., 2019), highlighting strong interregional variability. Future research should aim at identifying and gathering observational data of aragonite producers, to better constrain aragonite surface production rates, magnitudes and distribution. In shallow environments, future research should focus on quantifying the extent and response to environmental changes of aragonite muds (Geyman et al., 2022). As discussed above, the shut-off of shallow

aragonite mud factories would act as a negative feedback mechanism against climate changes on short time scales, that is, years to decades.

Another area of improvement is the need to better understand the dynamic equilibrium constituted by simultaneous aragonite dissolution and calcite precipitation. We were unfortunately unable to detect calcite concentration changes using XRPD, due to the small quantity of calcite that could have precipitated. Visualizing precipitates using scanning electron microscopy (Fuhr et al., 2022; Hartmann et al., 2023; Hover et al., 2001) could be key to understand the preferred locations of recrystallization and infer the phase that is precipitating. Performing dissolution experiments in C and O isotopically labeled seawater would allow to visualize and quantify the extent and rate of precipitation, for example, using a NanoSIMS (Akse et al., 2020).

Next to laboratory simulations, more in situ aragonite dissolution research at the seafloor is required to better understand CaCO₃ dynamics. The inconsistency between CaCO₃ dissolution rates in the lab and field shows the lack of understanding of the role of inhibitors, which makes it difficult for lab simulations to accurately represent actual deep-sea conditions. Unfortunately, the limited spatial and temporal resolution of instruments able to function in the deep sea makes observing aragonite dissolution at the seafloor difficult, which means models are often favored. However, multiple studies report a large discrepancy between in situ and model rate constants (Morse & Mackenzie, 1990). We believe micro-electrodes could be a very powerful tool in the future research of CaCO₃ dynamics due to their non-destructive small tips and high spatial resolution, especially when applied at the actual seafloor.

5. Conclusions

The goal of the rotating disk reactor experiment was to investigate the effect of aragonite dissolution on sediment-water TA fluxes under hydrodynamic conditions representative of benthic environments. It is likely aragonite dissolution caused an increase in pH and saturation state, even when the reactive surface area of the aragonite was relatively small. The galvanizing effect of aragonite caused increasing aragonite dissolution rates associated with decreasing calcite dissolution rates, resulting in a constant net TA flux, as calcite and aragonite dissolution rates compensated each other.

The second experiment involved a laboratory simulation of aragonite dissolution at the seafloor in the absence of flow. Coupled with our model, results are consistent with the hypothesis that the dissolution of the more soluble aragonite can lead to seawater supersaturation with respect to calcite. This means calcite dissolution could be suppressed in the top layer of the seabed and, according to our simulations, calcite precipitation can occur. This galvanizing effect was measured at high spatial resolution in a small cuvette using pH micro-electrodes, which have been proven to be a useful tool in studying benthic CaCO₃ dynamics. Initially, pteropod dissolution caused an increase in pH along the SWI, leading to seawater supersaturation with respect to calcite. After 1 day, pH dropped in both the sediment and water column. This observed effect could only be reproduced within our model by increasing the precipitation rate of calcite by a factor of more than 10⁵ to $411 \text{ mol} \cdot (\text{m}^3 \cdot \text{day})^{-1} \cdot [\text{Calcite}] \cdot (1 - \Omega_{\text{ca}})^{1.76}$.

Growing evidence for this galvanizing effect of aragonite dissolution on calcite suggests studies on marine CaCO₃ dynamics should incorporate the simultaneous presence of several carbonate minerals. This study suggests the presence of aragonite complicates our interpretation of the calcite lysocline and that more soluble carbonate phases should therefore be considered when interpreting the depth distribution of a given carbonate mineral. Spatial variety in aragonite accumulation could explain regional differences in paleo-acidification records, and will also affect carbonate sediments in the future as ocean acidification weakens the aragonite buffering effect and causes shoaling of the calcite saturation horizon.

Data Availability Statement

All data and code used to calculate the carbonate system using and create the plots in this paper are available in the GitHub repository at https://github.com/hannavdmortel/Ar_dissolution_HvdM (last access: 8 January 2024) and is archived on Zenodo at <https://doi.org/10.5281/zenodo.7805268> (van de Mortel, 2023). PyCO2SYS v1.8.0 (Humphreys et al., 2022) was used to solve for the carbonate system, with software available at <https://doi.org/10.5281/zenodo.3744275> (Humphreys et al., 2023). RADiv1 was used to model the dissolution and precipitation of

calcium carbonate (Sulpis, Humphreys, et al., 2022), with software available at <https://doi.org/10.5281/zenodo.4739205> (Sulpis, Humphreys, Wilhelmus, et al., 2022). Figures were made with Python version 3.9 (van Rossum & Drake Jr, 2009).

Acknowledgments

We thank Peter Kraal for his assistance at NIOZ, Geert-Jan Brummer for providing calcite sand and pteropods and Furu Mienis for providing cold-water coral samples. We thank Thom Claessen for his help in the UU Geolab. We thank Cecile Hilgen for her transportation services from the UU to NIOZ. We thank Anton Trammer from NIOZ Yerseke for lending and assisting with the Visisens TD system. We thank Olga Zygadłowska for explaining the Unisense software and helpful advice, as well as Caroline Slomp for lending the microprofiling system. This research was supported by the Netherlands Organisation for Scientific Research (NWO-XS Grant OCEANW.XS3.059 and NWO-VENI Grant VI.Veni.212.086 to O.S.) and the Netherlands Earth System Science Center. This project has received funding from the European Research Council (ERC) under the European Union's Horizon 2020 research and innovation programme (Grant agreement 819588) to M. Wolthers.

References

- Adkins, J. F., Naviaux, J. D., Subhas, A. V., Dong, S., & Berelson, W. M. (2021). The dissolution rate of CaCO₃ in the ocean. *Annual Reviews*, 13(1), 57–80. <https://doi.org/10.1146/ANNUREV-MARINE-041720-092514>
- Akse, S. P., Middelburg, J. J., King, H. E., & Polerecky, L. (2020). Rapid post-mortem oxygen isotope exchange in biogenic silica. *Geochimica et Cosmochimica Acta*, 284, 61–74. <https://doi.org/10.1016/j.gca.2020.06.007>
- Archer, D. (1996). An atlas of the distribution of calcium carbonate in sediments of the deep sea. *Global Biogeochemical Cycles*, 10(1), 159–174. <https://doi.org/10.1029/95GB03016>
- Aumont, O., Ethé, C., Tagliabue, A., Bopp, L., & Gehlen, M. (2015). PISCES-v2: An ocean biogeochemical model for carbon and ecosystem studies. *Geoscientific Model Development*, 8(8), 2465–2513. <https://doi.org/10.5194/gmd-8-2465-2015>
- Bednaršek, N., Bednaršek, N., Možina, J., Vogt, M., O'Brien, C., & Tarling, G. A. (2012). The global distribution of pteropods and their contribution to carbonate and carbon biomass in the modern ocean. *Earth System Science Data*, 4(1), 167–186. <https://doi.org/10.5194/ESSD-4-167-2012>
- Berelson, W. M., Anderson, R. F., Dymond, J., Demaster, D., Hammond, D. E., Collier, R., et al. (1997). Biogenic budgets of particle rain, benthic remineralization and sediment accumulation in the equatorial Pacific. *Deep-Sea Research Part II Topical Studies in Oceanography*, 44(9–10), 2251–2282. [https://doi.org/10.1016/S0967-0645\(97\)00030-1](https://doi.org/10.1016/S0967-0645(97)00030-1)
- Berelson, W. M., Hammond, D. E., McManus, J., & Kilgore, T. E. (1994). Dissolution kinetics of calcium carbonate in equatorial Pacific sediments. *Global Biogeochemical Cycles*, 8(2), 219–235. <https://doi.org/10.1029/93GB03394>
- Berger, W. H. (1967). Foraminiferal ooze: Solution at depths. *Science*, 156(3773), 383–385. <https://doi.org/10.1126/SCIENCE.156.3773.383>
- Berger, W. H. (1978). Deep-sea carbonate: Pteropod distribution and the aragonite compensation depth. *Deep-Sea Research*, 25(5), 447–452. [https://doi.org/10.1016/0146-6291\(78\)90552-0](https://doi.org/10.1016/0146-6291(78)90552-0)
- Berner, R. A. (1977). In N. R. Anderson & A. Malahoff (Eds.), *The fate of fossil fuel CO₂ in the oceans*. Springer. <https://doi.org/10.1007/978-1-4899-5016-1>
- Berner, R. A., & Honjo, S. (1981). Pelagic sedimentation of aragonite: Its geochemical significance. *Science*, 211(4485), 940–942. <https://doi.org/10.1126/SCIENCE.211.4485.940>
- Bischoff, W. D., Mackenzie, F. T., & Bishop, F. C. (1987). Stabilities of synthetic magnesian calcites in aqueous solution: Comparison with biogenic materials. *Geochimica et Cosmochimica Acta*, 51(6), 1413–1423. [https://doi.org/10.1016/0016-7037\(87\)90325-5](https://doi.org/10.1016/0016-7037(87)90325-5)
- Boeuf, D., Edwards, B. R., Eppley, J. M., Hu, S. K., Poff, K. E., Romano, A. E., et al. (2019). Biological composition and microbial dynamics of sinking particulate organic matter at abyssal depths in the oligotrophic open ocean. *Proceedings of the National Academy of Sciences of the United States of America*, 116(24), 11824–11832. <https://doi.org/10.1073/PNAS.1903080116/-DCSUPPLEMENTAL>
- Boudreau, B. P., & Guinasso, N. L. (1982). In K. A. Fanning & F. T. Manheim (Eds.), *The dynamic environment of the ocean floor*. Lexington Books.
- Boudreau, B. P., Middelburg, J. J., & Luo, Y. (2018). The role of calcification in carbonate compensation. *Nature Geoscience*, 11(12), 894–900. <https://doi.org/10.1038/s41561-018-0259-5>
- Boyle, E. A. (1983). Manganese carbonate overgrowths on foraminifera tests. *Geochimica et Cosmochimica Acta*, 47(10), 1815–1819. [https://doi.org/10.1016/0016-7037\(83\)90029-7](https://doi.org/10.1016/0016-7037(83)90029-7)
- Broecker, W. S., & Peng, T. (1982). *Tracers in the sea*. Eldigio Press.
- Bruni, S. F., & Wenk, H. (1985). Replacement of aragonite by calcite in sediments from the san Cassiano formation (Italy). *Journal of Sedimentary Research*, 55(2), 159–170. <https://doi.org/10.1306/212f8652-2b24-11d7-8648000102c1865d>
- Buchardt, B., & Weiner, S. (1981). Diagenesis of aragonite from upper Cretaceous ammonites: A geochemical case-study. *Sedimentology*, 28(3), 423–438. <https://doi.org/10.1111/j.1365-3091.1981.tb01691.x>
- Buitenhuis, E. T., Le Quéré, C., Bednaršek, N., & Schiebel, R. (2019). Large contribution of pteropods to shallow CaCO₃ export. *Global Biogeochemical Cycles*, 33(3), 458–468. <https://doi.org/10.1029/2018GB006110>
- Burton, E. A., & Walter, L. M. (1990). The role of pH in phosphate inhibition of calcite and aragonite precipitation rates in seawater. *Geochimica et Cosmochimica Acta*, 54(3), 797–808. [https://doi.org/10.1016/0016-7037\(90\)90374-T](https://doi.org/10.1016/0016-7037(90)90374-T)
- Butler, B. M., & Hillier, S. (2021). Automated full-pattern summation of x-ray powder diffraction data for high-throughput quantification of clay-bearing mixtures. *Clays and Clay Minerals*, 69(1), 38–51. <https://doi.org/10.1007/s42860-020-00105-6>
- Carter, W. P. (1978). Adsorption of amino acid-containing organic matter by calcite and quartz. *Geochimica et Cosmochimica Acta*, 42(8), 1239–1242. [https://doi.org/10.1016/0016-7037\(78\)90117-5](https://doi.org/10.1016/0016-7037(78)90117-5)
- Chave, K. E. (1954). Aspects of the biogeochemistry of magnesium I. Calcareous marine organisms. *The Journal of Geology*, 62(3), 266–283. <https://doi.org/10.1086/626162>
- Collen, J. D., & Burgess, C. J. (1979). Calcite dissolution, overgrowth and recrystallization in the benthic foraminiferal genus *notorotalia*. *Journal of Paleontology*, 53(6), 1343–1353.
- Comeau, S., Gattuso, J. P., Nisumaa, A. M., & Orr, J. (2012). Impact of aragonite saturation state changes on migratory pteropods. *Proceedings of Biological Sciences*, 279(1729), 732–738. <https://doi.org/10.1098/RSPB.2011.0910>
- De Kanel, J., & Morse, J. W. (1978). The chemistry of orthophosphate uptake from seawater on to calcite and aragonite. *Geochimica et Cosmochimica Acta*, 42(9), 1335–1340. [https://doi.org/10.1016/0016-7037\(78\)90038-8](https://doi.org/10.1016/0016-7037(78)90038-8)
- DelValls, T. A., & Dickson, A. G. (1998). The pH of buffers based on 2-amino-2-hydroxymethyl-1,3-propanediol ('tris') in synthetic sea water. *Deep Sea Research Part I: Oceanographic Research Papers*, 45(9), 1541–1554. [https://doi.org/10.1016/S0967-0637\(98\)00019-3](https://doi.org/10.1016/S0967-0637(98)00019-3)
- Dickson, A. G. (1990). Standard potential of the reaction: AgCl(s) + 1/2H₂(g) = Ag(s) + HCl(aq), and the standard acidity constant of the ion HSO₄⁻ in synthetic sea water from 273.15 to 318.15 K. *The Journal of Chemical Thermodynamics*, 22(2), 113–127. [https://doi.org/10.1016/0021-9614\(90\)90074-Z](https://doi.org/10.1016/0021-9614(90)90074-Z)
- Dickson, A. G., & Riley, J. P. (1979). The estimation of acid dissociation constants in sea-water media from potentiometric titrations with strong base. II. The dissociation of phosphoric acid. *Marine Chemistry*, 7(2), 101–109. [https://doi.org/10.1016/0304-4203\(79\)90002-1](https://doi.org/10.1016/0304-4203(79)90002-1)
- Dickson, A. G., Sabine, C. L., & Christian, J. R. (2007). Guide to best practices for ocean CO₂ measurements.

- Dong, S., Berelson, W. M., Rollins, N. E., Subhas, A. V., Naviaux, J. D., Celestian, A. J., et al. (2019). Aragonite dissolution kinetics and calcite/ aragonite ratios in sinking and suspended particles in the North Pacific. *Earth and Planetary Science Letters*, *515*, 1–12. <https://doi.org/10.1016/j.epsl.2019.03.016>
- Egleston, E. S., Sabine, C. L., & Morel, F. M. M. (2010). Revelle revisited: Buffer factors that quantify the response of ocean chemistry to changes in DIC and alkalinity. *Global Biogeochemical Cycles*, *24*(1). <https://doi.org/10.1029/2008GB003407>
- Ellis, D. B., & Moore, T. C. J. (1973). Calcium carbonate, opal, and quartz in holocene pelagic sediments and the calcite compensation level in the South Atlantic ocean. *Journal of Marine Research*.
- Fabry, V. J. (1990). Shell growth rates of pteropod and heteropod molluscs and aragonite production in the open ocean: Implications for the marine carbonate system. *Journal of Marine Research*, *48*(1), 209–222. <https://doi.org/10.1357/00224090784984614>
- Fabry, V. J., & Deuser, W. G. (1991). Aragonite and magnesian calcite fluxes to the deep Sargasso Sea. *Deep-Sea Research, Part A: Oceanographic Research Papers*, *38*(6), 713–728. [https://doi.org/10.1016/0198-0149\(91\)90008-4](https://doi.org/10.1016/0198-0149(91)90008-4)
- Feely, R. A., Sabine, C. L., Lee, K., Berelson, W., Kleypas, J., Fabry, V. J., & Millero, F. J. (2004). Impact of anthropogenic CO₂ on the CaCO₃ system in the oceans. *Science*, *305*(5682), 362–366. <https://doi.org/10.1126/SCIENCE.1097329>
- Friedlingstein, P., Jones, M. W., O'Sullivan, M., Andrew, R. M., Bakker, D. C. E., Hauck, J., et al. (2022). Global carbon budget 2021. *Earth System Science Data*, *14*(4), 1917–2005. <https://doi.org/10.5194/ESSD-14-1917-2022>
- Fuhr, M., Geilert, S., Schmidt, M., Liebetrau, V., Vogt, C., Ledwig, B., & Wallmann, K. (2022). Kinetics of olivine weathering in seawater: An experimental study. *Frontiers in Climate*, *4*, 39. <https://doi.org/10.3389/FCLIM.2022.831587/BIBTEX>
- Fukuhara, T., Tanaka, Y., Ioka, N., & Nishimura, A. (2008). An in situ experiment of calcium carbonate dissolution in the central Pacific Ocean. *International Journal of Greenhouse Gas Control*, *2*(1), 78–88. [https://doi.org/10.1016/S1750-5836\(07\)00085-0](https://doi.org/10.1016/S1750-5836(07)00085-0)
- Gangstø, R., Gehlen, M., Schneider, B., Bopp, L., Aumont, O., & Joos, F. (2008). Modeling the marine aragonite cycle: Changes under rising carbon dioxide and its role in shallow water CaCO₃ dissolution. *Biogeosciences*, *5*(4), 1057–1072. <https://doi.org/10.5194/BG-5-1057-2008>
- Gardner, J., Manno, C., Bakker, D. C. E., Peck, V. L., & Tarling, G. A. (2018). Southern Ocean pteropods at risk from ocean warming and acidification. *Marine Biology*, *165*(1), 8. <https://doi.org/10.1007/S00227-017-3261-3>
- Geyman, E. C., Wu, Z., Nadeau, M. D., Edmonson, S., Turner, A., Purkis, S. J., et al. (2022). The origin of carbonate mud and implications for global climate. *Proceedings of the National Academy of Sciences of the United States of America*, *119*(43), e2210617119. https://doi.org/10.1073/PNAS.2210617119/SUPPL_FILE/PNAS.2210617119.SD06.CSV
- Goff, J. A., Jenkins, C. J., & Jeffress Williams, S. (2008). Seabed mapping and characterization of sediment variability using the usSEABED data base. *Continental Shelf Research*, *28*(4–5), 614–633. <https://doi.org/10.1016/J.CSR.2007.11.011>
- Gruber, N., Clement, D., Carter, B. R., Feely, R. A., Van Heuven, S., Hoppema, M., et al. (2019). The oceanic sink for anthropogenic CO₂ from 1994 to 2007. *Science (New York, N.Y.)*, *363*(6432), 1193–1199. <https://doi.org/10.1126/SCIENCE.AAU5153>
- Gutjahr, A., Dabringhaus, H., & Lacmann, R. (1996). Studies of the growth and dissolution kinetics of the CaCO₃ polymorphs calcite and aragonite II. The influence of divalent cation additives on the growth and dissolution rates. *Journal of Crystal Growth*, *158*(3), 310–315. [https://doi.org/10.1016/0022-0248\(95\)00447-5](https://doi.org/10.1016/0022-0248(95)00447-5)
- Hartmann, J., Suitner, N., Lim, C., Schneider, J., Marin-Samper, L., Aristegui, J., et al. (2023). Stability of alkalinity in ocean alkalinity enhancement (OAE) approaches: Consequences for durability of CO₂ storage. *Biogeosciences*, *20*(4), 781–802. <https://doi.org/10.5194/BG-20-781-2023>
- Hauri, C., Friedrich, T., & Timmermann, A. (2015). Abrupt onset and prolongation of aragonite undersaturation events in the Southern Ocean. *Nature Climate Change*, *6*(2), 172–176. <https://doi.org/10.1038/nclimate2844>
- Haynes, L. L., & Hönisch, B. (2020). The seawater carbon inventory at the Paleocene-Eocene thermal maximum. *Proceedings of the National Academy of Sciences of the United States of America*, *117*(39), 24088–24095. https://doi.org/10.1073/PNAS.2003197117/SUPPL_FILE/PNAS.2003197117.SD05.XLSX
- Honjo, S., & Erez, J. (1978). Dissolution rates of calcium carbonate in the deep ocean; an in-situ experiment in the North Atlantic Ocean. *Earth and Planetary Science Letters*, *40*(2), 287–300. [https://doi.org/10.1016/0012-821X\(78\)90099-7](https://doi.org/10.1016/0012-821X(78)90099-7)
- Hover, V. C., Walter, L. M., & Peacor, D. R. (2001). Early marine diagenesis of biogenic aragonite and Mg-calcite: New constraints from high-resolution STEM and AEM analyses of modern platform carbonates. *Chemical Geology*, *175*(3–4), 221–248. [https://doi.org/10.1016/S0009-2541\(00\)00326-0](https://doi.org/10.1016/S0009-2541(00)00326-0)
- Hülsemann, J. (1966). On the routine analysis of carbonates in unconsolidated sediments. *Journal of Sedimentary Research*, *36*(2), 622–625.
- Humphreys, M. P., Lewis, E. R., Sharp, J. D., & Pierrot, D. (2022). PyCO2SYS v1.8: Marine carbonate system calculations in Python. *Geoscientific Model Development*, *15*(1), 15–43. <https://doi.org/10.5194/GMD-15-15-2022>
- Humphreys, M. P., & Matthews, R. S. (2022). Calculate: Total alkalinity from titration data in Python (v23.3) software. *Zenodo*. <https://doi.org/10.5281/ZENODO.6684203>
- Humphreys, M. P., Schiller, A. J., Sandborn, D., Gregor, L., Pierrot, D., Van Heuven, S. M. A. C., et al. (2023). PyCO2SYS: Marine carbonate system calculations in Python (v1.8.2) [software]. *Zenodo*. <https://doi.org/10.5281/zenodo.7550236>
- Ilyina, T., Six, K. D., Segsneider, J., Maier-Reimer, E., Li, H., & Núñez-Riboni, I. (2013). Global ocean biogeochemistry model HAMOCC: Model architecture and performance as component of the MPI-Earth system model in different CMIP5 experimental realizations. *Journal of Advances in Modeling Earth Systems*, *5*(2), 287–315. <https://doi.org/10.1029/2012MS000178>
- Janiszewska, K., Mazur, M., Machalski, M., & Stolarski, J. (2018). From pristine aragonite to blocky calcite: Exceptional preservation and diagenesis of cephalopod naere in porous Cretaceous limestones. *PLoS One*, *13*(12), e0208598. <https://doi.org/10.1371/journal.pone.0208598>
- Johnson, K. M., & Hofmann, G. E. (2020). Combined stress of ocean acidification and warming influence survival and drives differential gene expression patterns in the Antarctic pteropod, *Limacina helicina* Antarctica. *Conservation Physiology*, *8*(1). <https://doi.org/10.1093/CONPHYS/COAA013>
- Johnson, K. M., Hoshijima, U., Sugano, C. S., Nguyen, A. T., & Hofmann, G. E. (2016). Shell dissolution observed in *Limacina helicina* Antarctica from the Ross Sea, Antarctica: Paired shell characteristics and in situ seawater chemistry. *Preprint*. <https://doi.org/10.5194/bg-2016-467>
- Keir, R. S. (1980). The dissolution kinetics of biogenic calcium carbonates in seawater. *Geochimica et Cosmochimica Acta*, *44*(2), 241–252. [https://doi.org/10.1016/0016-7037\(80\)90135-0](https://doi.org/10.1016/0016-7037(80)90135-0)
- Lalli, C. M., & Gilmer, R. W. (1989). *Pelagic snails: The biology of holoplanktonic gastropod mollusks*. Stanford University Press. Retrieved from https://books.google.com/books/about/Pelagic_Snails.html?id=y1Afwz5cxPMC
- Lewis, E., & Wallace, D. W. R. (1998). Program developed for CO₂ system calculations. *ORNL/CDIAC*, *105*. <https://doi.org/10.15485/1464255>
- Lorens, R. B. (1981). Sr, Cd, Mn and Co distribution coefficients in calcite as a function of calcite precipitation rate. *Geochimica et Cosmochimica Acta*, *45*(4), 553–561. [https://doi.org/10.1016/0016-7037\(81\)90188-5](https://doi.org/10.1016/0016-7037(81)90188-5)

- Lueker, T. J., Dickson, A. G., & Keeling, C. D. (2000). Ocean pCO₂ calculated from dissolved inorganic carbon, alkalinity, and equations for K₁ and K₂: Validation based on laboratory measurements of CO₂ in gas and seawater at equilibrium. *Marine Chemistry*, 70(1–3), 105–119. [https://doi.org/10.1016/S0304-4203\(00\)00022-0](https://doi.org/10.1016/S0304-4203(00)00022-0)
- Mackenzie, F. T., Bischoff, W. D., Bishop, F. C., Loijens, M., Schoonmaker, J., & Wollast, R. (1983). *Mg-Calcites: Low temperature occurrence, solubility and solid-solution behavior*. In R. J. Reeder (Ed.), *Carbonates: Mineralogy and chemistry* (Vol. 11, pp. 97–143). Mineralogical Society of America.
- Middelburg, J. J. (2019). Marine carbon biogeochemistry: A primer for earth system scientists. *Springer Briefs in Earth System Sciences*, 126. <https://doi.org/10.1007/978-3-030-10822-9>
- Millero, F., Huang, F., Zhu, X., Liu, X., & Zhang, J.-Z. (2001). Adsorption and desorption of phosphate on calcite and aragonite in seawater. *Aquatic Geochemistry*, 7.
- Millero, F. J. (1979). The thermodynamics of the carbonate system in seawater. *Geochimica et Cosmochimica Acta*, 43(10), 1651–1661. [https://doi.org/10.1016/0016-7037\(79\)90184-4](https://doi.org/10.1016/0016-7037(79)90184-4)
- Milliman, J. D. (1975). Dissolution of aragonite, Mg-calcite, and calcite in the North Atlantic ocean. *Geology*, 3(8), 461–462. [https://doi.org/10.1130/0091-7613\(1975\)3<461:doamac>2.0.co;2](https://doi.org/10.1130/0091-7613(1975)3<461:doamac>2.0.co;2)
- Milliman, J. D. (1993). Production and accumulation of calcium carbonate in the ocean: Budget of a nonsteady state. *Global Biogeochemical Cycles*, 7(4), 927–957. <https://doi.org/10.1029/93GB02524/FORMAT/PDF>
- Moore, J. K., Lindsay, K., Doney, S. C., Long, M. C., & Misumi, K. (2013). Marine ecosystem dynamics and biogeochemical cycling in the community earth system model [CESM1(BGC)]: Comparison of the 1990s with the 2090s under the RCP4.5 and RCP8.5 scenarios. *Journal of Climate*, 26(23), 9291–9312. <https://doi.org/10.1175/JCLI-D-12-00566.1>
- Morse, J. W., & Mackenzie, F. T. (1990). *Geochemistry of sedimentary carbonates*. Elsevier. Retrieved from https://books.google.com/books/about/Geochemistry_of_Sedimentary_Carbonates.html?id=3Cvk2lkukgEC
- Mucci, A. (1983). The solubility of calcite and aragonite in seawater at various salinities, temperatures, and one atmosphere total pressure. *American Journal of Science*, 283(7), 780–799. <https://doi.org/10.2475/AJS.283.7.780>
- Mucci, A., & Morse, J. W. (1984). The solubility of calcite in seawater solutions of various magnesium concentration, It = 0.697 m at 25°C and one atmosphere total pressure. *Geochimica et Cosmochimica Acta*, 48(4), 815–822. [https://doi.org/10.1016/0016-7037\(84\)90103-0](https://doi.org/10.1016/0016-7037(84)90103-0)
- Naviaux, J. D., Subhas, A. V., Dong, S., Rollins, N. E., Liu, X., Byrne, R. H., et al. (2019). Calcite dissolution rates in seawater: Lab vs. in-situ measurements and inhibition by organic matter. *Marine Chemistry*, 215, 103684. <https://doi.org/10.1016/J.MARCHEM.2019.103684>
- Orr, J. C., Epitalon, J. M., Dickson, A. G., & Gattuso, J. P. (2018). Routine uncertainty propagation for the marine carbon dioxide system. *Marine Chemistry*, 207, 84–107. <https://doi.org/10.1016/J.MARCHEM.2018.10.006>
- Orr, J. C., Fabry, V. J., Aumont, O., Bopp, L., Doney, S. C., Feely, R. A., et al. (2005). Anthropogenic ocean acidification over the twenty-first century and its impact on calcifying organisms. *Nature*, 437, 681–686. <https://doi.org/10.1038/nature04095>
- Palmer, T. J., & Wilson, M. A. (2004). Calcite precipitation and dissolution of biogenic aragonite in shallow Ordovician calcite seas. *Lethaia*, 37(4), 417–427. <https://doi.org/10.1080/00241160410002135>
- Paulsen, M. L., & Dickson, A. G. (2020). Preparation of 2-amino-2-hydroxymethyl-1,3-propanediol (TRIS) pHT buffers in synthetic seawater. *Limnology and Oceanography: Methods*, 18(9), 504–515. <https://doi.org/10.1002/LOM3.10383>
- Pearson, P. N., Evans, S. L., & Evans, J. (2015). Effect of diagenetic recrystallization on the strength of planktonic foraminifer tests under compression. *Journal of Micropalaeontology*, 34(1), 59–64. <https://doi.org/10.1144/jmpaleo2013-032>
- Peijnenburg, K. T. C. A., Janssen, A. W., Wall-Palmer, D., Goetze, E., Maas, A. E., Todd, J. A., & Marlétaz, F. (2020). The origin and diversification of pteropods precede past perturbations in the Earth's carbon cycle. *Proceedings of the National Academy of Sciences of the United States of America*, 117(41), 25609–25617. https://doi.org/10.1073/PNAS.1920918117/SUPPL_FILE/PNAS.1920918117.SD01.XLSX
- Peterson, M. N. A. (1966). Calcite: Rates of dissolution in a vertical profile in the central Pacific. *Science*, 154(3756), 1542–1544. <https://doi.org/10.1126/SCIENCE.154.3756.1542>
- Plummer, L. N., Wigley, T. M. L., & Parkhurst, D. L. (1978). The kinetics of calcite dissolution in CO₂-water systems at 5 degrees to 60 degrees C and 0.0 to 1.0 atm CO₂. *American Journal of Science*, 278(2), 179–216. <https://doi.org/10.2475/AJS.278.2.179>
- Reeder, R. J. (1983). Crystal chemistry of the rhombohedral carbonates. In R. J. Reeder (Ed.), *Carbonates: Mineralogy and chemistry* (pp. 1–47). Mineralogical Society of America.
- Richardson, T. L. (2019). Mechanisms and pathways of small-phytoplankton export from the surface ocean. *Annual Review of Marine Science*, 11(1), 57–74. <https://doi.org/10.1146/ANNUREV-MARINE-121916-063627>
- Sarazin, G., Michard, G., & Prevot, F. (1999). A rapid and accurate spectroscopic method for alkalinity measurements in sea water samples. *Water Research*, 33(1), 290–294. [https://doi.org/10.1016/S0043-1354\(98\)00168-7](https://doi.org/10.1016/S0043-1354(98)00168-7)
- Schink, D. R., & Guinasso, N. L. (1977). Modeling the influence of bioturbation and other processes on carbonate dissolution on the sea floor. In N. R. Anderson & A. Malahoff (Eds.), *The fate of fossil fuel CO₂ in the oceans*.
- Silver, M. W., Shanks, A. L., & Trent, J. D. (1978). Marine snow: Microplankton habitat and source of small-scale patchiness in pelagic populations. *Science*, 201(4353), 371–373. <https://doi.org/10.1126/SCIENCE.201.4353.371>
- Sjöberg, E. L., & Rickard, D. (1983). The influence of experimental design on the rate of calcite dissolution. *Geochimica et Cosmochimica Acta*, 47(12), 2281–2285. [https://doi.org/10.1016/0016-7037\(83\)90051-0](https://doi.org/10.1016/0016-7037(83)90051-0)
- Sjöberg, E. L., & Rickard, D. T. (1984a). Calcite dissolution kinetics: Surface speciation and the origin of the variable pH dependence. *Chemical Geology*, 42(1–4), 119–136. [https://doi.org/10.1016/0009-2541\(84\)90009-3](https://doi.org/10.1016/0009-2541(84)90009-3)
- Sjöberg, E. L., & Rickard, D. T. (1984b). Temperature dependence of calcite dissolution kinetics between 1 and 62°C at pH 2.7 to 8.4 in aqueous solutions. *Geochimica et Cosmochimica Acta*, 48(3), 485–493. [https://doi.org/10.1016/0016-7037\(84\)90276-X](https://doi.org/10.1016/0016-7037(84)90276-X)
- Smith, S. V., & Mackenzie, F. T. (2016). The role of CaCO₃ reactions in the contemporary oceanic CO₂ cycle. *Aquatic Geochemistry*, 22(2), 153–175. <https://doi.org/10.1007/S10498-015-9282-Y>
- Štulík, K., Amatore, C., Holub, K., Mareček, V., & Kutner, W. (2000). Microelectrodes. Definitions, characterization, and applications (Technical report). *Pure and Applied Chemistry*, 72(8), 1483–1492. <https://doi.org/10.1351/PAC200072081483>
- Subhas, A. V., Rollins, N. E., Berelson, W. M., Dong, S., Erez, J., & Adkins, J. F. (2015). A novel determination of calcite dissolution kinetics in seawater. *Geochimica et Cosmochimica Acta*, 170, 51–68. <https://doi.org/10.1016/J.GCA.2015.08.011>
- Sulpis, O., Agrawal, P., Wolthers, M., Munhoven, G., Walker, M., & Middelburg, J. J. (2022). Aragonite dissolution protects calcite at the seafloor. *Nature Communications*, 13(1), 1–8. <https://doi.org/10.1038/s41467-022-28711-z>
- Sulpis, O., Boudreau, B. P., Mucci, A., Jenkins, C., Trossman, D. S., Arbic, B. K., & Key, R. M. (2018). Current CaCO₃ dissolution at the seafloor caused by anthropogenic CO₂. *Proceedings of the National Academy of Sciences of the United States of America*, 115(46), 11700–11705. <https://doi.org/10.1073/PNAS.1804250115/-DCSUPPLEMENTAL>

- Sulpis, O., Humphreys, M. P., Wilhelmus, M. M., & Carroll, D. (2022). Radi.m: The reactive-advective-diffusive-irrigative diagenetic sediment module in MATLAB/GNU Octave (0.2). Zenodo [software]. <https://doi.org/10.5281/zenodo.4739205>
- Sulpis, O., Humphreys, M. P., Wilhelmus, M. M., Carroll, D., Berelson, W. M., Menemenlis, D., et al. (2022). RADiv1: A non-steady-state early diagenetic model for ocean sediments in Julia and MATLAB/GNU octave. *Geoscientific Model Development*, 15(5), 2105–2131. <https://doi.org/10.5194/GMD-15-2105-2022>
- Sulpis, O., Jeansson, E., Dinauer, A., Lauvset, S. K., & Middelburg, J. J. (2021). Calcium carbonate dissolution patterns in the ocean. *Nature Geoscience*, 14(6), 423–428. <https://doi.org/10.1038/S41561-021-00743-Y>
- Sulpis, O., Mucci, A., Boudreau, B. P., Barry, M. A., & Johnson, B. D. (2019). Controlling the diffusive boundary layer thickness above the sediment–water interface in a thermostated rotating-disk reactor. *Limnology and Oceanography: Methods*, 17(4), 241–253. <https://doi.org/10.1002/LOM3.10309>
- Takahashi, T., & Broecker, W. S. (1977). In N. R. Anderson & A. Malahoff (Eds.), *Mechanisms for calcite dissolution on the sea floor*.
- Takahashi, T., Sutherland, S. C., Chipman, D. W., Goddard, J. G., Ho, C., Newberger, T., et al. (2014). Climatological distributions of pH, pCO₂ (2), total CO₂, alkalinity, and CaCO₃ saturation in the global surface ocean, and temporal changes at selected locations. *Marine Chemistry*, 164, 95–125. <https://doi.org/10.1016/j.marchem.2014.06.004>
- Turekian, K. K. (1956). Rapid technique for determination of carbonate content of deep-sea cores: Geological notes. *AAPG Bulletin*, 40(10), 2507–2509. <https://doi.org/10.1306/5CEAE5B0-16BB-11D7-8645000102C1865D>
- Uppström, L. R. (1974). The boron/chlorinity ratio of deep-sea water from the Pacific Ocean. *Deep Sea Research and Oceanographic Abstracts*, 21(2), 161–162. [https://doi.org/10.1016/0011-7471\(74\)90074-6](https://doi.org/10.1016/0011-7471(74)90074-6)
- Van De Mortel, H. (2023). hannavdmortel/Ar_dissolution_HvdM: v1.2 (v1.2) dataset. Zenodo. <https://doi.org/10.5281/zenodo.7805268>
- Van Rossum, G., & Drake Jr, F. L. (2009). Python 3 reference manual. *Software*.
- Volk, T., & Hoffert, M. I. (1985). Ocean carbon pumps: Analysis of relative strengths and efficiencies in Ocean-driven atmospheric CO₂ changes. *The Carbon Cycle and Atmospheric CO*, 99–110. <https://doi.org/10.1029/GM032P0099>
- Wall-Palmer, D., Janssen, A. W., Goetze, E., Choo, L. Q., Mekkes, L., & Peijnenburg, K. T. C. A. (2020). Fossil-calibrated molecular phylogeny of Atlantid heteropods (Gastropoda, Pterotracheoidea). *BMC Evolutionary Biology*, 20(1), 1–14. <https://doi.org/10.1186/S12862-020-01682-9/TABLES/3>
- Watanabe, S., Hajima, T., Sudo, K., Nagashima, T., Takemura, T., Okajima, H., et al. (2011). MIROC-ESM 2010: Model description and basic results of CMIP5–20c3m experiments. *Geoscientific Model Development*, 4(4), 845–872. <https://doi.org/10.5194/GMD-4-845-2011>
- Westphal, H. (2006). Limestone–marl alternations as environmental archives and the role of early diagenesis: A critical review. *International Journal of Earth Sciences*, 95(6), 947–961. <https://doi.org/10.1007/s00531-006-0084-8>
- Wilson, R. W., Millero, F. J., Taylor, J. R., Walsh, P. J., Christensen, V., Jennings, S., & Grosell, M. (2005). Contribution of fish to the marine inorganic carbon cycle. *Science*, 323(5912), 359–362. <https://doi.org/10.1126/science.1157972>
- Zachos, J. C., Röhl, U., Schellenberg, S. A., Sluijs, A., Hodell, D. A., Kelly, D. C., et al. (2005). Paleoclimate: Rapid acidification of the ocean during the paleocene-eocene thermal maximum. *Science*, 308(5728), 1611–1615. https://doi.org/10.1126/SCIENCE.1109004/SUPPL_FILE/ZACHOS.SOM.PDF
- Zeebe, R. E., & Wolf-Gladrow, D. A. (2001). *CO₂ in seawater: Equilibrium, kinetics, isotopes* (1st ed.). Elsevier Science.
- Ziveri, P., Gray, W. R., Anglada-Ortiz, G., Manno, C., Grelaud, M., Incarbona, A., et al. (2023). Pelagic calcium carbonate production and shallow dissolution in the North Pacific Ocean. *Nature Communications*, 14(1), 1–14. <https://doi.org/10.1038/S41467-023-36177-W>
- Zuddas, P., & Mucci, A. (1998). Kinetics of calcite precipitation from seawater: II. The influence of the ionic strength. *Geochimica et Cosmochimica Acta*, 62(5), 757–766. [https://doi.org/10.1016/S0016-7037\(98\)00026-X](https://doi.org/10.1016/S0016-7037(98)00026-X)